Controlled Flight of a Microrobot Powered by Soft Artificial Muscles

The first controlled flight of a microrobot powered by soft artificial muscles

Yufeng Chen[1,2*], Huichan Zhao[3], Jie Mao[1,4], Pakpong Chirarattananon[5], E. Farrell Helbling[1,2], Nak-seung Patrick Hyun[1,2], David R. Clarke[1], & Robert J. Wood[1,2*]

[1]John A. Paulson School of Engineering and Applied Sciences, Harvard University, Cambridge, Massachusetts 02138, USA. [2]Wyss Institute for Biologically Inspired Engineering, Harvard University, Cambridge, Massachusetts 02138, USA. [3]Department of Mechanical Engineering, Tsinghua University, Beijing 100084, China. [4]Department of Chemical and Biochemical Engineering, Zhejiang University, Hangzhou 310027, China. [5]Department of Mechanical and Biomedical Engineering, City University of Hong Kong, Kowloon, Hong Kong, China.

[*]Corresponding authors

Flying insects capable of navigating in highly cluttered natural environments can withstand in-flight collisions because of the combination of their low inertia[1] and the resilience of their wings[2], exoskeletons[1], and muscles. Current insect-scale (<10 cm, <5 g) aerial robots[3-6] use rigid microscale actuators, which are typically fragile under external impact. Biomimetic artificial muscles[7-10] capable of large deformation offer a promising alternative for actuation because they can endure the stresses caused by such impacts. However, existing soft actuators[11-13] have not yet demonstrated sufficient power density for liftoff, and their actuation nonlinearity and limited bandwidth further create challenges for achieving closed-loop flight control. Here we develop the first heavier-than-air aerial robots powered by soft artificial muscles that demonstrate open-loop, passively stable ascending flight as well as closed-loop, hovering flight. The robots are driven by 100 mg, multi-layered dielectric elastomer actuators (DEA) that have a resonant frequency and power density of 500 Hz and 600 W/kg, respectively. To increase actuator output mechanical power and to demonstrate flight control, we present strategies to overcome challenges unique to soft actuators, such as nonlinear transduction and dynamic buckling. These robots can sense, and withstand, collisions with surrounding obstacles, and can recover from in-flight collisions by exploiting material robustness and vehicle passive stability. We further perform a simultaneous flight with

two micro-aerial-vehicles (MAV) in cluttered environments. These robots rely on offboard amplifiers and an external motion capture system to provide power to the DEAs and control flights. Our work demonstrates how soft actuators can achieve sufficient power density and bandwidth to enable controlled flight, illustrating the vast potential of developing next-generation agile soft robots.

Soft robotics[14-16] is an emerging field aiming to develop versatile systems that can safely interact with humans and manipulate delicate objects in unstructured environments. A major challenge in building soft-actuated mobile robots involves developing muscle-like actuators that have high energy density, bandwidth, robustness, and lifetime. Previous studies have described soft actuators that can be actuated chemically[17], pneumatically[18,19], hydraulically[20], thermally[21,22], or electrically[7,23]. Among these soft transducers, DEAs have shown a combination of muscle-like energy density and bandwidth[8], enabling the development of biomimetic robots capable of terrestrial[11,24,25] and aquatic locomotion[26,27]. However, while there is growing interest in developing heavier-than-air, soft-actuated aerial robots, existing soft robots[11-13] have been unable to achieve liftoff due to limited actuator power density (<200 W/kg), bandwidth (<20 Hz), and difficulties of integration with rigid robotic structures such as transmission and wings.

To enable controlled hovering flight of a soft-actuated robot, we identify and address two major challenges: developing a soft actuator with sufficient power density (>200 W/kg) and designing driving and control strategies to account for actuation nonlinearity (see Methods section 1 for details on vehicle design and DEA performance requirements). First, we develop a multi-layered, compact DEA that has a power density of 600 W/kg without requiring pre-strain. Second, we integrate the DEA into a light-weight, flapping wing mechanism and utilize system resonance to remove higher harmonics induced by the nonlinear transduction. In combination, we design a 155 mg flapping-wing module that can be assembled into several configurations. Using these modules, we are able to construct vehicles that not only demonstrate passively stable ascending flight but also controlled hovering flight.

Our robot is driven by a multi-layered DEA rolled into a cylindrical shell to generate linear actuation

(see Methods section 2 for details on DEA fabrication). The DEA is mounted in a light-weight airframe (Fig. 1a), with the two ends of the DEA attached to planar four-bar transmissions. This design allows one DEA to simultaneously actuate two wings in an analogous manner as the indirect flight muscles in neopteran flying insects[28]. By using the planar four-bar transmissions, the DEA's axial extension and contraction are converted into the wing's rotational stroke motion (Fig. 1b). In quasi-static operation, the actuation is unidirectional because DEA strain is proportional to the square of the applied electric field. In dynamic operation, the DEA extends and contracts due to its intrinsic inertia and stiffness, yet its elongation amplitude is larger than the retraction amplitude. To ensure the mean wing stroke (α) motion is symmetric with respect to the robot body, the resting wing stroke plane is offset by approximately 15° (Fig. 1b) during robot assembly. The DEA is pre-strained by 2% when it is attached to the robot transmissions, and this pre-strain loads the elastic four-bar transmissions to introduce the wing stroke bias. This small pre-strain does not noticeably change the DEA performance, and this design is advantageous compared to artificial flight muscles with a large pre-strain[11] (>100%) because it does not require a rigid and heavy supporting structure. In this way, the robot wing stroke (α) motion is fully controlled by the actuator, whereas the wing pitch (β) rotation is passively mediated by the compliant wing hinge (Fig. 1c). Figure 1d and Supplementary Video 1 show a half flapping period actuated at 280 Hz. The tracked wing stroke and pitch motion for the same experiment are shown in figure 1e. Based on an aerodynamic model developed in a previous study[29], we estimate that this flapping motion will generate a net lift force of approximately 1.8 mN, corresponding to 1.2 times the robot weight. This modular robot can be assembled into several configurations to demonstrate different flight capabilities. For instance, figure 1f shows micro-aerial vehicles driven by one (center), two (left), and four DEAs (right). These vehicles exhibit open loop liftoff (one DEA), stable ascending flight (two DEAs), and hovering flight through feedback control (four DEAs), respectively.

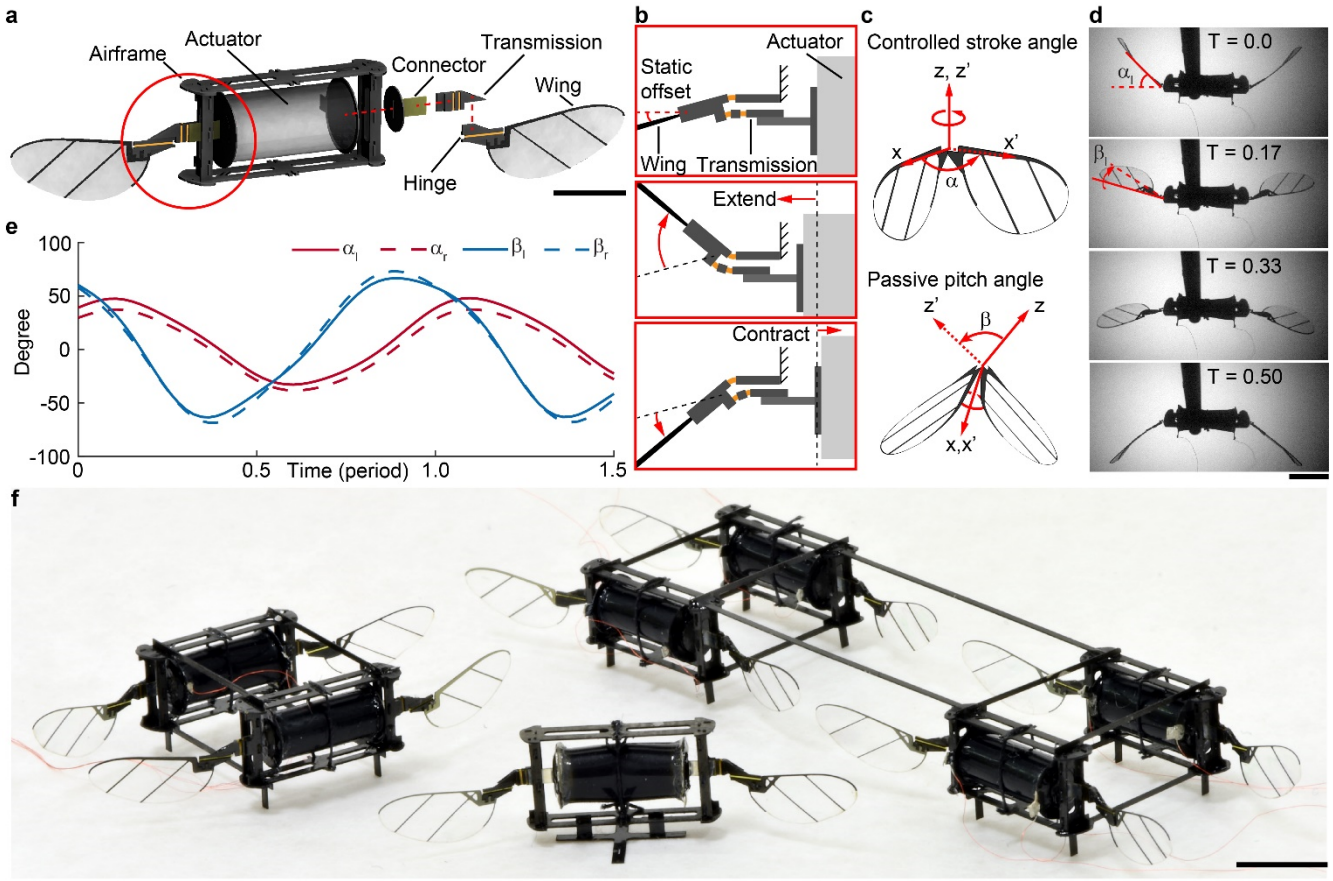

Figure 1 | Robot design and flapping wing kinematics. **a,** A CAD model of a 155 mg flapping wing robot driven by a dielectric elastomer actuator (DEA). The exploded view of the robot's right half shows the actuator, connector, four-bar transmission, wing, and wing hinge. The circled region of the robot's left transmission is magnified in **b**. **b,** Enlarged top view of the robot's actuator-transmission-wing assembly. The DEA is pre-strained by 2% when it is attached to the robot's transmissions, which induces a static stroke angle bias of approximately 15°. The linear DEA actuation is translated into the rotational wing stroke motion. **c,** Illustrations of the actively controlled wing stroke (α) motion and the passive wing pitch (β) motion. **d,** An image sequence of the flapping wing motion operated at 280 Hz. The time is normalized to a flapping period. The wing stroke rotation (α_l) induces passive wing pitch rotation (β_l). **e,** Tracked flapping wing kinematics that correspond to the experiment shown in **d**. The wing stroke (red) amplitudes of the left (solid line) and the right (dotted line) wings are 42 and 41 degrees, respectively. The wing pitch (blue) amplitudes of the left (solid line) and the right (dotted line) wings are 57 and 61 degrees, respectively. **f,** Image of flapping wing microrobots driven by a single actuator, two actuators, and four actuators. Scale bars (**a, d, f**) represent 5 mm.

To achieve flight of a soft-actuated robot, the DEA must have sufficient power density and the robot transmissions and wings must be designed around the actuator's output force, displacement, and bandwidth. In contrast to previous studies[11] that developed pre-strained acrylic DEAs to achieve large deformation (>30%) and high energy density (>4 J/kg) but low bandwidth (<30 Hz), we use a silicone elastomer as the dielectric material for the flight muscles to achieve higher bandwidth (>400 Hz), combined with moderate strain (10-15%) and energy density (1.13 J/kg). For driving frequencies lower than 600 Hz, our DEA's blocked force (Fig. 2a) is independent of frequency because its electrical

properties are tuned to have a small RC time constant of 0.18 ms. The DEA's free displacement (Fig. 2b) peaks at 15% strain when it is driven at 500 Hz. The free displacement amplitude includes the contribution from the first and higher order harmonics in response to a sinusoidal driving signal. We observe a secondary peak of free displacement (Fig. 2b) when the driving frequency is 250 Hz, due to exciting the second order harmonic that is near the resonant frequency (500 Hz). Our robot design utilizes the first harmonic to drive the flapping wing motion. By computing the Fast Fourier Transform (FFT) of the DEA's response to a white noise, we quantify the magnitude (Fig. 2c) and phase (Fig. 2d) of the linear part of its response. When operated at the takeoff condition (300 Hz, 1300 V), the DEA has a power density of 300 W/kg and a lifetime of over 600,000 cycles. (see Methods section 3 for details on actuator characterization).

Powering MAVs using soft actuators shows an advantage over the state-of-the-art flapping wing microrobots (< 10 cm, < 5 g) driven by rigid actuators such as piezoelectric bimorphs[3] and electromagnetic motors[5]. Although microrobotic components, such as the airframe, transmissions, and wings, are robust to collisions (because inertial contributions diminish at the millimeter scale), rigid micro-actuators are fragile — particularly the piezoceramic actuators (fracture strength and failure strain are 120 MPa and 0.3%, respectively) used in many similarly sized devices[3,4]. In contrast, this DEA driven microrobot is robust to collisions. For instance, when one wing collides with an obstacle (Fig. 2e and Supplementary Video 2), the impact is absorbed by the DEA because of its high compliance and resilience. In addition, the DEA can detect collisions (Fig. 2f) through concomitant actuation and sensing under similar principles to that of electromagnetic motors[30] and piezoelectric actuators[31]. Similarly, if an obstacle directly hits the DEA during its actuation (Fig. 2g and Supplementary Video 2), the DEA deformation can also be detected by monitoring the current (Fig. 2h). These experiments show that DEA is not only robust to collisions, but also is capable of sensing collisions with the environment (see Supplementary Information S1 for more experimental results on collision sensing).

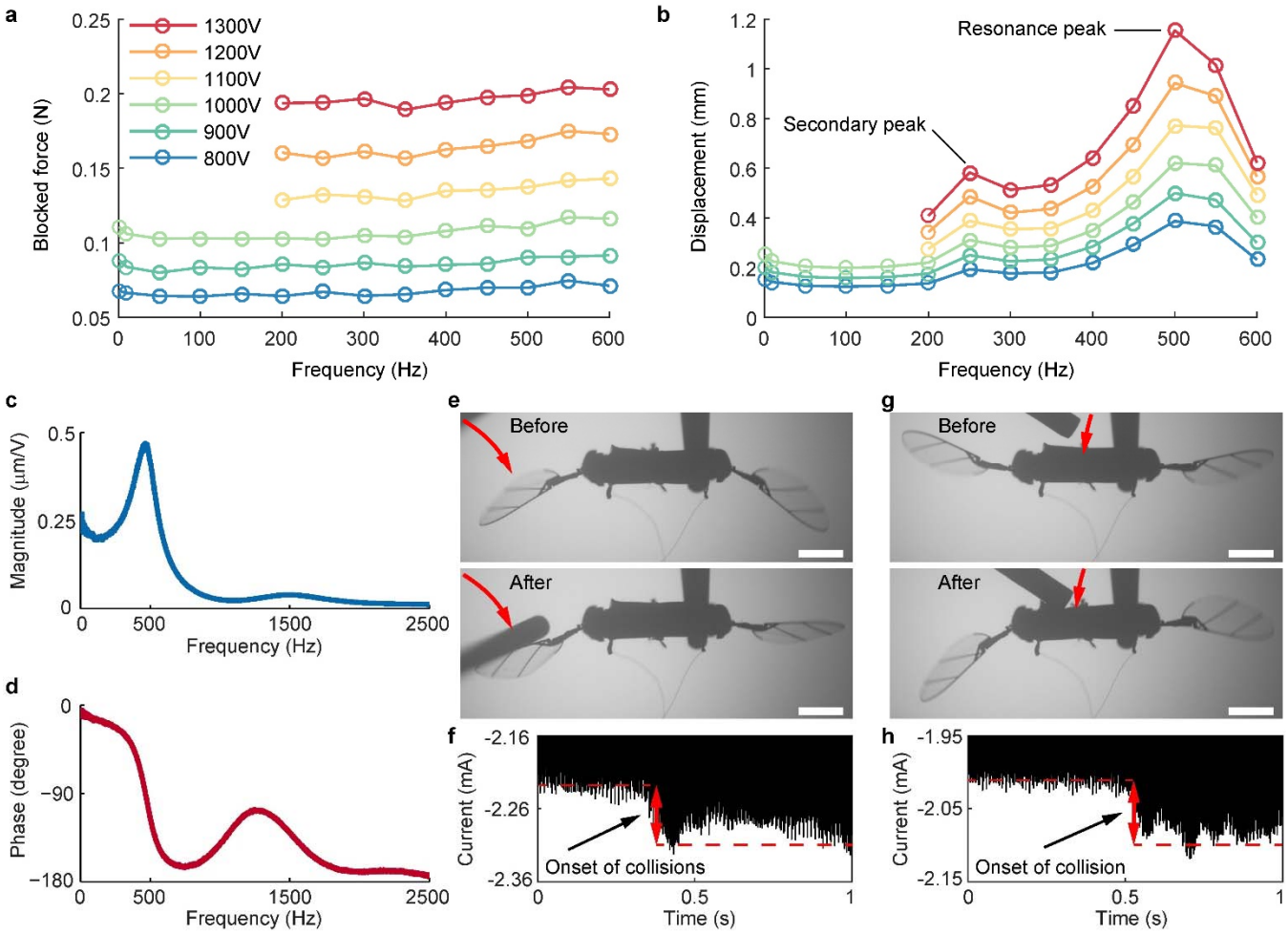

Figure 2 | DEA performance, robustness, and collision sensing. a, b, Measured DEA blocked force (**a**) and free displacement (**b**) as functions of operating frequency and voltage amplitude. In **a** and **b**, there are no experiments conducted for the cases combining low frequency (<200 Hz) and high voltage (>1000 V) because the elastomer cannot endure a large electric field at low frequencies. **c, d,** Frequency response of the DEA free displacement under an input voltage of 600 V. **c** and **d** show the magnitude and phase of the frequency response, respectively. **e,** A flapping wing repeatedly collides with an obstacle when the DEA is operated at 320 Hz and 1350V. **f,** Measured DEA current as a function of time. The jump in the DEA current indicates the onset of the wing-obstacle collisions. **g,** A rigid object presses down on the DEA that is operating at 320 Hz and 1300 V. **h,** The jump in the measured DEA current indicates the time that the object makes contact with the DEA. Scale bars (**e**, **g**) are 5 mm.

Despite having favorable properties such as robustness and self-sensing, DEAs present challenges for achieving flight due to their inherent nonlinearity. The strain in a DEA is proportional to the square of the applied electric field[7]. Consequently, a sinusoidal driving signal does not result in symmetric up stroke and down stroke motion (Fig. 3a and Supplementary Video 3) due to the influence of higher order harmonics (see Supplementary Information S2 for details on nonlinear actuation and higher harmonics). For example, when operated at 100 Hz, the wing down stroke exhibits a slow reversal from T = 0.5 to T = 0.7 (Fig. 3a and Supplementary Video 3). According to a previous aerodynamic study[29], this slow wing

reversal can result in a substantial reduction in lift force. To mitigate the up stroke and down stroke asymmetry, we drive the DEA near the resonant frequency of the DEA-transmission-wing system to amplify the fundamental harmonic and attenuate higher harmonics. This asymmetry is substantially reduced when the DEA is driven at a frequency that is higher than half its resonance. Compared to flapping motion at 1 Hz or 100 Hz, the slow wing reversal is negligible when the driving frequency increases to 280 Hz (Fig. 3b and Supplementary Video 3).

In addition to exhibiting nonlinear transduction, the DEA can undergo dynamic buckling that substantially affects flapping motion and reduces the lift force. When operated near the system resonance, the DEA experiences a large compressive load due to the drag force from the robot wing. This normal load causes the DEA to buckle along a direction perpendicular to its actuation axis. The actuator returns to its nominal configuration as this compressive load is reduced during wing reversal. In the next flapping period, the DEA buckles in the opposite direction due to the momentum of the restoring motion. Dynamic buckling substantially reduces the wing stroke amplitude (Fig. 3c-d and Supplementary Video 3), and it occurs at half the flapping frequency (Fig. 3d and Supplementary Video 3). Further, the large DEA deformation causes excessive electrode self-clearing and substantially reduces DEA performance and lifetime. Dynamic buckling can be inhibited by using circumferential constraints (in this case strings) to limit the DEA's off-axis motion at its mid-plane (Fig. 3e). Figure 3f shows the left-wing stroke amplitude as a function of driving frequency and voltage. The kinks of the green lines indicate stroke amplitude reduction due to dynamic buckling. Constraining the DEA's off-axis motion enables higher driving voltages and frequencies, which correspond to higher wing stroke amplitudes. The red shaded region indicates operating conditions that are inaccessible without constraining the DEA. Adding constraints increases the wing stroke peak-to-peak amplitude by approximately 25°, leading to a 1.6 times increase in lift force.

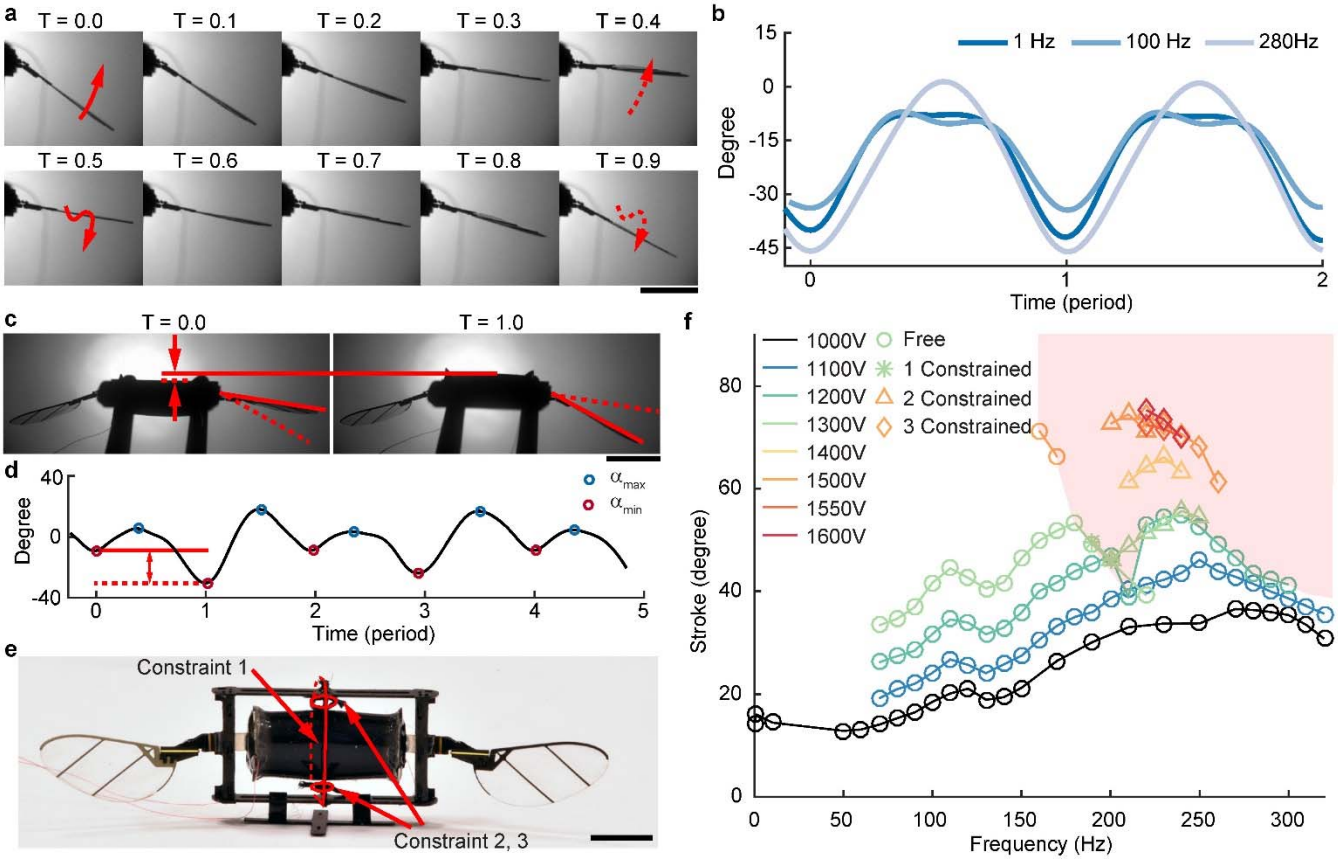

Figure 3 | DEA nonlinearity and dynamic buckling. a, Image sequence of the robot flapping motion at 100 Hz for one flapping period. The up stroke and down stroke are asymmetric. **b,** Tracked wing stroke motion at 1 Hz, 100 Hz, and 280 Hz. The wing stroke motion is asymmetric at low flapping frequencies. The nonlinear high frequency modes are reduced by post-resonant inertial effects. **c,** Images that illustrate the DEA dynamic buckling. The red lines indicate that the DEA buckles and the wing stroke amplitude reduces. **d,** Tracked wing stroke motion that corresponds to the experiment shown in **c**. The wing stroke amplitude reduces and the flapping period halves. **e,** Three pieces of thread circumferentially constrain the DEA to the robot airframe to eliminate out-of-plane motion and inhibit dynamic buckling. **f,** Stroke amplitude as a function of driving voltage and frequency. The shaded region (red) represents the stroke amplitudes and flapping frequencies that are unachievable without constraining the DEA. Scale bars (**a**, **c, e**) represent 5 mm.

Addressing the challenges of nonlinear actuation enables flight demonstrations of the DEA-driven, flapping-wing microrobots. While all flight demonstrations are unconstrained, the robots carry a thin tether for offboard power supply and control. Driven by a single DEA, the 155 mg robot demonstrates open-loop liftoff. The net lift generated by this MAV is approximately 1.8 mN, and it reaches a maximum height of 1.5 cm in 90 ms (Fig. 4a and Supplementary Video 4). To mitigate aerodynamic torque imbalances due to fabrication and assembly imprecision, a carbon fiber rod with a point mass is attached to the robot's airframe to adjust its center of mass position. However, without attitude and position control authority, this intrinsically unstable robot flips over within 110 ms of liftoff.

166 To demonstrate stable ascending flight, we build a two actuator, four-winged robot (Fig. 1e) that utilizes
167 precession around the body z-axis to achieve passive stability. We bias the resting wing pitch angle during
168 robot assembly to induce a net yaw torque around the robot's body z-axis. The body z-component of the
169 angular momentum induced by precession rejects the robot's pitch and roll torque imbalances. In an open
170 loop takeoff experiment, we demonstrate that the robot reaches a height of 23.5 cm within 0.83 seconds
171 of open-loop takeoff (Fig. 4b and Supplementary Video 5). We also construct a dynamical model and use
172 numerical simulation to confirm the experimental observation on passive upright stability. Our simulation
173 (Fig. 4c) shows the robot ascends 22.7 cm in 0.83 seconds with a yaw rate of 17.2 rev/s. This passive
174 stability property further enables us to operate more than one robot in a confined space without the need
175 of motion tracking and feedback control. We demonstrate simultaneous takeoff flights of two robots
176 (Supplementary Video 6) and show that they are robust against collisions with the surroundings and each
177 other. In addition, passive stability and collision robustness can provide the ability to recover from in-
178 flight collisions or disturbances. Figure 4d and Supplementary Video 6 show a collision recovery flight in
179 which the robot takes off from the center of a cylindrical shell, collides with the shell wall during its ascent,
180 and continues to fly upward after making the collision. However, passive in-flight collision recovery is a
181 probabilistic event that depends on the robot's flight speed and the collision impact. Without any robot
182 attitude sensing and feedback control, the robot may be destabilized after experiencing one or multiple
183 collisions (see Supplementary Information S3 for a detailed discussion on passive stability, collision
184 recovery, and additional flight results).

185 To demonstrate controlled hovering flight, we design a four actuator, eight-winged robot (Fig. 1e) and
186 use a motion tracking system[3] and off-board computation for sensing and control (see Supplementary
187 Information S4 for details on the controller design, implementation, experimental validation, and
188 repeatability). Figure 4e shows composite images of a 16-second hovering flight, and the red dot indicates
189 the desired setpoint. Figure 4f shows the corresponding trajectory of the same flight (Supplementary Video

7), and the color scale represents the distance from the current position to the setpoint. For this 16-second flight, the maximum deviation of altitude, lateral position, and body angles are 12 mm (0.2 body length (BL)), 36 mm (0.6 BL), and 9°, respectively (Fig. 4g-i).

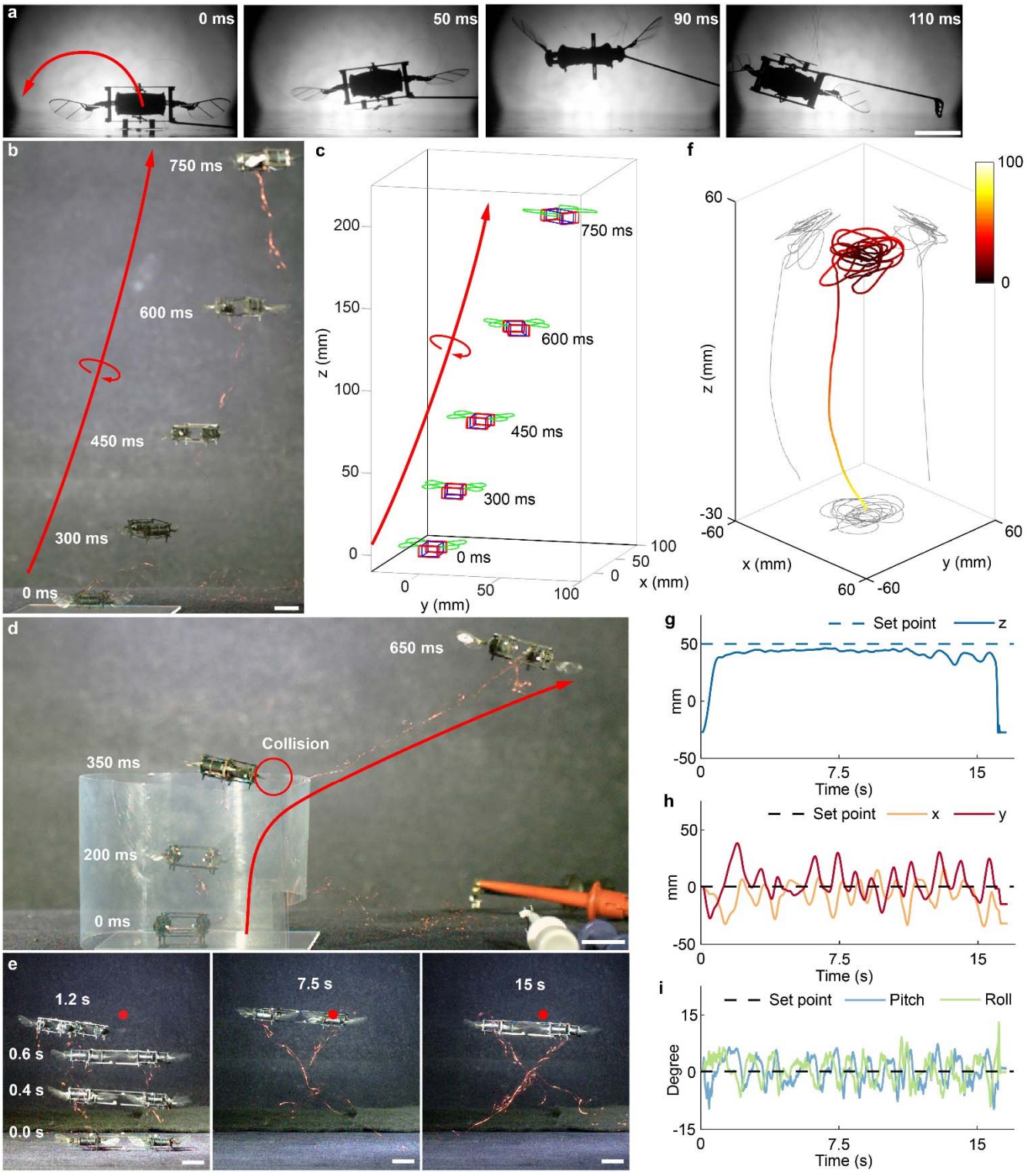

Figure 4 | Robot flight demonstrations. a, Unstable liftoff of a 155 mg robot driven by one DEA. The robot reaches a height of 1.5 cm and then flips upside down due to unstable body pitch rotation. **b, c,** Passively stable ascending flight of a 320 mg robot driven by two DEAs. Both the experiment (**b**) and the dynamical simulation (**c**) show the robot reaches approximately 23 cm within 0.75 s of open-loop takeoff. The simulation shows the robot precesses at a yaw rate of 17.2 rev/s. **d,** The 320 mg robot remains passively upright stable after colliding with an obstacle and continues to fly upward. **e,** Composite images of a 16-second controlled hovering flight that is demonstrated by a 660 mg robot driven by four DEAs. **f,** The tracked flight trajectory corresponding to the experiment in **e**. The color scale denotes the distance between the robot position and the set point. (**g-i**), Robot altitude (**g**), x and y positions (**h**), and attitude (**i**) as functions of time. Scale bars (**a**, **b, d, e**) are 1 cm.

To summarize, these flight demonstrations show the first time that soft artificial muscles have sufficient power density to enable liftoff and have adequate bandwidth for flight control. Compared to the state-of-the-art MAVs driven by microscale rigid actuators (<500 mg), these soft actuator robots show advantages such as in-flight robustness to collisions and self-sensing. A feature of the DEA's fabrication scalability is that it enables efficient production of robotic modules that can be assembled in different configurations for different functions. These properties will be important for enabling swarm flight of MAVs in highly cluttered environments where collisions are difficult to avoid. However, compared to a recent piezoelectric-actuator-driven MAV[32] that can demonstrate power-autonomous takeoff flights, this robot consumes 15 times more input power and requires a drive voltage 6.5 times higher. The robot's weight and net lift are 170% and 75% that of the state-of-the-art piezoelectric-driven vehicle. To enable power autonomous flight in soft aerial robots, future studies need to reduce a soft actuator's operating voltage, improve its power efficiency, and further increase its power density. Reducing actuation voltage is crucial because up to 75% of the input electrical power can be dissipated by compact high-voltage boost and drive circuitry (as in a recent power autonomous MAV[32]). This challenge of lowering driving voltage can be tackled by refining DEA multi-layering techniques to further reduce the elastomer layer's thickness. Towards improving transduction efficiency, future studies can incorporate new architectures of electrically actuated soft actuators such as the electrohydraulic Peano-HASEL[33] actuators that can use flexible metallic electrodes to reduce resistive losses. To increase power density, new electroactive polymers with higher dielectric strengths and lower viscoelasticity should be explored and incorporated into future soft artificial flight muscles. From a robot design perspective, scaling the vehicle size up can substantially mitigate the challenges associated with achieving power autonomy. A larger vehicle size can provide a larger net payload, which allows the robot to carry a larger and more efficient boost circuit. In addition, scaling up the wing size corresponds to a reduction of operating frequency, and leads to a linear increase in the DEA's power efficiency (see Methods section 3 and Supplementary Information S5 for a detailed discussion on future directions to achieve power autonomous flights). More broadly and

significantly, our work demonstrates that soft-actuated robots can be agile, robust, and controllable. These characteristics are important for developing future generations of soft robots for diverse applications such as environmental exploration and manipulation.

References

1 Dickerson, A.K., Shankles, P.G., Madhavan, N.M. & Hu, D.L. Mosquitoes survive raindrop collisions by virtue of their low mass. *Proceedings of the National Academy of Sciences* **109**, 9822-9827 (2012).

2 Mountcastle, A. M. & Combes, S. A. Biomechanical strategies for mitigating collision damage in insect wings: structural design versus embedded elastic materials. *Journal of Experimental Biology* **217**, 1108–1115 (2014).

3 Ma, K. Y., Chirarattananon, P., Fuller, S. B. & Wood, R. J. Controlled flight of a biologically inspired, insect-scale robot. *Science* **340**, 603-607 (2013).

4 Chen, Y. *et al.* A biologically inspired, flapping-wing, hybrid aerial-aquatic microrobot. *Science Robotics* **2**, eaao5619 (2017).

5 Zou, Y., Zhang, W. & Zhang, Z. Liftoff of an electromagnetically driven insect-inspired flapping-wing robot. *IEEE Transactions on Robotics* **32**, 1285-1289 (2016).

6 De Croon, G., De Clercq, K., Ruijsink, R., Remes, B. & De Wagter, C. Design, aerodynamics, and vision-based control of the DelFly. *International Journal of Micro Air Vehicles* **1**, 71-97 (2009).

7 Carpi, F., Bauer, S., & Rossi, D. D. Stretching dielectric elastomer performance. *Science* **330**, 1759-1761 (2010).

8 Rosset, S. & Shea, H. R. Flexible and stretchable electrodes for dielectric elastomer actuators. *Applied Physics A* **110**, 281-307 (2013).

9 Zhao, H. *et al.* Compact dielectric elastomer linear actuators. *Advanced Functional Materials* **28**, 1804328 (2018).

10 Acome, E., *et al*. Hydraulically amplified self-healing electrostatic actuators with muscle-like performance. *Science* **359**, 61-65 (2018).

11 Pelrine, R. *et al.* Dielectric elastomer artificial muscle actuators: toward biomimetic motion. in *Smart Structures and Materials 2002: Electroactive polymer actuators and devices (EAPAD).* 126-138 (2002).

12 Zhao, J., Niu, J., McCoul, D., Leng, J. & Pei, Q. A rotary joint for a flapping wing actuated by dielectric elastomers: design and experiment. *Meccanica* **50**, 2815-2824 (2015).

13 Lau, G.-K., Lim, H.-T., Teo, J.-Y. & Chin, Y.-W. Lightweight mechanical amplifiers for rolled dielectric elastomer actuators and their integration with bio-inspired wing flappers. *Smart Materials and Structures* **23**, 025021 (2014).

14 Shepherd, R. F. *et al.* Multigait soft robot. *Proceedings of the national academy of sciences* **108**, 20400-20403 (2011).

15 Rus, D. & Tolley, M. T. Design, fabrication and control of soft robots. *Nature* **521**, 467 (2015).

16 Majidi, C. Soft robotics: a perspective—current trends and prospects for the future. *Soft Robotics* **1**, 5-11 (2014).

17 Choe, K. *et al.* Performance Characteristics of Electro–chemically Driven Polyacrylonitrile Fiber Bundle Actuators. *Journal of intelligent material systems and structures* **17**, 563-576 (2006).
18 Suzumori, K., Iikura, S. & Tanaka, H. Applying a flexible microactuator to robotic mechanisms. *IEEE Control systems magazine* **12**, 21-27 (1992).
19 Onal, C. D., Chen, X., Whitesides, G. M. & Rus, D. Soft mobile robots with on-board chemical pressure generation. in *Robotics Research* 525-540 (2017).
20 Katzschmann, R. K., Marchese, A. D. & Rus, D. Hydraulic autonomous soft robotic fish for 3D swimming. in *Experimental Robotics.* 405-420 (2016).
21 Loomis, J., Xu, P. & Panchapakesan, B. Stimuli-responsive transformation in carbon nanotube/expanding microsphere–polymer composites. *Nanotechnology* **24**, 185703 (2013).
22 Cheng, N. G., Gopinath, A., Wang, L., Iagnemma, K. & Hosoi, A. E. Thermally tunable, self-healing composites for soft robotic applications. *Macromolecular Materials and Engineering* **299**, 1279-1284 (2014).
23 Sadeghipour, K., Salomon, R. & Neogi, S. Development of a novel electrochemically active membrane and'smart'material based vibration sensor/damper. *Smart Materials and Structures* **1**, 172 (1992).
24 Pei, Q., Rosenthal, M., Stanford, S., Prahlad, H. & Pelrine, R. Multiple-degrees-of-freedom electroelastomer roll actuators. *Smart materials and structures* **13**, N86 (2004).
25 Shian, S., Bertoldi, K. & Clarke, D. R. Use of aligned fibers to enhance the performance of dielectric elastomer inchworm robots. in *Electroactive Polymer Actuators and Devices (EAPAD).* 94301P (2015).
26 Li, T. *et al.* Fast-moving soft electronic fish. *Science Advances* **3**, e1602045 (2017).
27 Berlinger, F. *et al.* A Modular Dielectric Elastomer Actuator to Drive Miniature Autonomous Underwater Vehicles. in *IEEE International Conference on Robotics and Automation (ICRA).* 3429-3435 (2018).
28 Dickinson, M. H. Muscle efficiency and elastic storage in the flight motor of Drosophila. *Science* **268**, 87-90 (1995).
29 Chen, Y., Gravish, N., Desbiens, A. L., Malka, R. & Wood, R. J. Experimental and computational studies of the aerodynamic performance of a flapping and passively rotating insect wing. *Journal of Fluid Mechanics* **791**, 1-33 (2016).
30 Tu. Z., Fei. F., Zhang. J. & Deng. X. Acting is Seeing: Navigating Tight Space Using Flapping Wings. in *IEEE International Conference on Robotics and Automation (ICRA)* (2019).
31 Jayaram, K., Jafferis, N. T., Doshi, N., Goldberg, B. & Wood, R. J. Concomitant sensing and actuation for piezoelectric microrobots. *Smart Materials and Structures* **27**, 065028 (2018).
32 Jafferis, N.T., Helbling, E.F., Karpelson, M. & Wood, R.J. Untethered flight of an insect-sized flapping-wing microscale aerial vehicle. *Nature* **570**, 491-495 (2019)
33 Kellaris, N., Venkata, V. G., Smith, G. M., Mitchell, S. K., & Keplinger, C. Peano-HASEL actuators: Muscle-mimetic, electrohydraulic transducers that linearly contract on activation. *Science Robotics*, **3(14)**, eaar3276.

Acknowledgement

We thank Yishan Zhu for comments and discussions. This work is supported by the National Science Foundation (award #CMMI-1830291) and the Wyss Institute for Biologically Inspired Engineering. In addition, the prototypes were enabled by equipment supported by the Army Research Office DURIP program (award no. W911NF-13-1-0311). Any opinions, findings, and conclusions or recommendations expressed in this material are those of the authors and do not necessarily reflect the views of the National Science Foundation.

Author Contribution

Y.C., H.Z., and R.J.W proposed and designed the research; Y.C., H.Z., and J.M. built the robot; Y.C., H.Z., J.M., P.C., and E.H. conducted the experimental work; Y.C., H.Z., P.C., N.P.H., D.C., and R.J.W contributed to modelling and data analysis; Y.C. wrote the paper. All authors provided feedback.

Data Availability

All data generated or analyzed for this paper are included in the published article, its Methods, and Supplementary Information. Original videos, computer code, and sensor data are available from the corresponding author on reasonable request.

Methods

1. Conceptual design of a DEA-powered aerial robot

The DEA-powered robot consists of five major components: an actuator, an airframe, transmission, two wing hinges, and two wings. The two ends of the DEA are connected to the robot transmission, and the DEA's linear actuation is converted to the flapping motion of both wings. The structural design of this robot is similar to that of a microrobot powered by piezoelectric actuators presented in a previous study[34]. However, we need to redesign each component to accommodate the soft actuator. In the following, we describe the design process to determine key robot parameters and present the requirements on DEA performance.

To achieve takeoff, the DEA must satisfy requirements for blocked force, resonant frequency, free displacement, and power density. Specifically, the actuator needs to meet two conditions. First, the robot wings need to flap at sufficient frequency with adequate amplitude to generate a lift force that balances the robot weight. This condition places requirements on the DEA's operating frequency and displacement. Rearranging the equation that imposes the lift force and robot weight balance leads to the relationship:

$$f\delta = \frac{1}{2\pi \hat{r}_2 R^2 T}\sqrt{\frac{AR\, W f_m}{\overline{C_L}\rho}}, \tag{1}$$

where f is the robot's operating frequency, δ is half of the DEA's free displacement at the frequency f, $\hat{r}_2$ is the wing's second area moment, R is the wing span, T is the transmission ratio, AR is the wing's aspect ratio, W is the robot weight, $\overline{C_L}$ is the mean lift coefficient, ρ is the air density, and f_m is a scaling ratio such that the extra lift force can be used for flight control. In addition to satisfying this kinematic condition, the DEA needs to overcome the aerodynamic drag force during flight, and this imposes a requirement on the DEA's blocked force:

$$F_B = 2\sqrt{2} T r_{cp} W f_m \frac{\overline{C_D}}{\overline{C_L}}, \tag{2}$$

where F_B is the DEA's blocked force, r_{cp} is the wing's spanwise center of pressure, and $\overline{C_D}$ is the time averaged drag coefficient. The derivation of equations (1) and (2) closely follows from equations (1-14) in a previous work[34]. In equations (1) and (2), we assume that the DEA's blocked force is independent of its actuation frequency. This assumption is validated in the next section on DEA characterization. Multiplying equations (1) and (2) gives a requirement for the DEA's output mechanical power.

The design of a DEA-powered aerial robot also needs to satisfy an additional condition because the DEA's actuation is nonlinear with respect to input voltage. With a sinusoidal input, the DEA's actuation contains higher order harmonics that can adversely affect flapping wing kinematics. As discussed in the main text, we attenuate higher order harmonics by setting the robot operating frequency close to the natural frequency of the DEA-transmission-wing system. A previous study[34] shows the actuator-transmission-wing system can be described by a lumped-parameter model. The system resonant frequency is given by:

$$f = 2\pi\sqrt{\frac{k_m + k_h T^2}{m_a + 2T^2 I_{zz}}}, \tag{3}$$

where k_m is the DEA's intrinsic stiffness, m_a is the DEA mass, k_h is the transmission's torsional stiffness, and I_{zz} is the wing's moment of inertia relative to the stroke rotational axis. For our robot, the transmission stiffness is much lower than the DEA's effective stiffness. To obtain a higher operating frequency, this condition requires a smaller wing moment of inertia. The wing moment of inertia can be decreased by reducing wing size. Using equations (1) - (3), we select values for the transmission ratio and the wing size while satisfying constraints imposed by our fabrication methods (i.e., minimum feature size, wing inertia, etc). The values of these design parameters are reported in Extended Data Table 1. Using these parameters, we obtain the following requirements for a 100 mg DEA: $F_B = 0.2$ N, $f = 290$ Hz, and $\delta = 0.3$ mm. Multiplying these parameters shows that the DEA needs to have a minimum output power density of 200 W/kg. This requirement is similar to that of the MAVs powered by piezoelectric actuators[3] and to the power density values estimated for flying insects.

2. Fabrication of robot components

The robot airframe, transmission, wings, and wing hinges are made using an existing multi-scale, multi-material fabrication method[35]. The airframe consists of eight pieces of 160 μm carbon fiber laminates assembled manually and reinforced with Loctite 495 (Extended Data Figure 1a). The robot transmission is a planar four-bar mechanism. The transmission ratio is approximated as $T = l_3^{-1}$, where the link length l_3 is marked in Extended Data Figure 1b. The robot transmission is attached to the DEA via a fiber glass connector, which insulates the robot structure from the DEA's driving signals. Further, the transmission connects the airframe and the wing hinge. A wing is attached onto the robot's wing hinge. The wing hinge and wing are designed based on an existing method[36], and their geometries are illustrated in Extended Data Figure 1c and d.

The DEA takes the form of a cylindrical shell, whose height and radius determine the actuation frequency, blocked force, and free displacement. The DEA is made of a multi-layering process[9], and it is rolled from a rectangular elastomer sheet that has embedded electrodes. Since the DEA drives two wings simultaneously, its free displacement needs to be larger than 600 μm (twice the value of the design parameter δ). Based on the values of DEA free displacement, peak loading, and elastomer stiffness, we set the actuator length to 8 mm. To obtain a blocked force over 0.2 N, the elastomer sheet (prior to roll up) width is set to 5 cm. This elastomer sheet is approximately 220 μm thick, and it is manually rolled into a cylindrical shell whose inner and outer diameters are 1.5 mm and 4.5 mm, respectively.

The elastomer is a 5:4 mixture of Ecoflex 0030 (Smooth-On) and Sylgard 184 (Dow Corning). The ratio of crosslinker in Sylgard 184 is 1:40. We put a thin layer of CNT (from Nano-C Inc, Westwood, MA) on the elastomer and use it as the DEA's compliant electrode. For coating the electrode, we use 150 μL of CNT solution over a 90 mm diameter PTFE filter (Satorius 7022P). The procedures for elastomer preparation, spin coating, and electrode patterning are adopted from a previous study[9].

We made several modifications to the fabrication process to increase DEA power density and endurance. First, DEA power density can be increased by having an even number of CNT layers. Extended Data Figure 1e shows the rolling process of a multi-layered DEA. We use grey colored regions to denote the elastomer layers. The positive and negative electrodes are represented by red and black lines, respectively. We represent the bottom elastomer layer with a darker grey color. When the elastomer sheet is rolled into a cylindrical shell, the DEA's bottom layer is put into contact with its top layer. This is illustrated by the inset shown in Extended Data Figure 1f. The region highlighted by blue lines further shows that a new layer is formed by the DEA's top and bottom elastomer layers and electrodes. If the top and bottom electrodes are oppositely charged (as illustrated in Extended Data Figure 1f), then this effective layer develops an electric field and contributes to actuation. We must have an even number of electrode layers to ensure the bottom and top electrodes are oppositely charged. In this work, our DEA design has six CNT and seven elastomer layers. Further, if the top and bottom elastomer layers have the same thickness as all other layers, then the electric field in this new layer is only half that of other layers because the effective layer thickness is $t_{top} + t_{bottom}$ (Extended Data Figure 1g). Hence, reducing the top and bottom layer thickness increases the electric field in the additional layer, and this results in an increase in DEA output power. We use a faster spin coating speed (2700 rpm) for the top and bottom layer and slower speed (1700 rpm) for the middle layers. Through reducing the top and bottom elastomer layer thickness by approximately 35% (Extended Data Figure 1h), we obtain an 11% mass reduction and a 9% increase in output power relative to a DEA with constant elastomer layer thickness. After making the elastomer layers and transferring the electrodes, we cut out the DEA from the elastomer substrate and roll it into a cylindrical shell. In the previous study[9], the DEA is cut out manually with a razor blade. Our application requires higher accuracy, so we program a digital cutter (Silhouette Cameo) to cut out the DEA. The DEA's length is set to 8.6 mm including the exposed CNT tabs for electrical connection. With this modification, variation in the DEA length is reduced to within 150 μm. Having a precise DEA length is crucial for attaching the DEA to the robot transmission during assembly.

In addition, the DEA's bandwidth depends on several factors such as elastomer mechanical viscoelasticity ($\tan\delta$), DEA geometry, and electrode conductivity. Here, we improve the fabrication process relative to a previous study[9] to ensure good conductivity during DEA actuation (Extended Data Figure 1i). After the DEA is rolled into a shell, carbon conductive adhesive (Electron Microscopy Sciences) is applied to the exposed electrodes and carbon fiber endcaps are glued to each end. For driving our flapping wing robot, the DEA needs to overcome aerodynamic drag during both elongation and retraction phases. During DEA retraction, aerodynamic drag opposes the DEA motion and applies a tensile stress on the DEA connections. At peak loading, this tensile stress weakens the bonding between the elastomer and the endcap, and it can create local tears and further lead to delamination. This delamination reduces electrical conductivity, which increases the DEA's time constant and reduces its bandwidth. We overcome this problem by modifying the fabrication process to increase the end cap adhesion strength. During fabrication, Loctite 416 is applied to the outer perimeter of the elastomer shell and the endcaps. The DEA is compressed with a mass of 18 g and then baked at 72 °C for 4 hours. The glue cures in this process and holds the electrical connections in compression. The preload is removed after the glue cures, and other regions of the DEA return to a neutral state. A photograph of the DEA is shown in Extended Data Figure 1j. With this procedure, we obtain an increase in DEA conductivity of approximately four times compared to those made using previous methods[9].

3. DEA performance characterization

Here we describe the experimental characterization of the DEA's blocked force, free displacement, bandwidth, power consumption, and efficiency. To measure the DEA's blocked force, we place the DEA under a force sensor (Nano 17 Titanium). The sensor is mounted on a two-axis stage and is lowered until it touches the DEA's top cap (Extended Data Figure 2a). To ensure the DEA remains securely affixed under the sensor during its retraction phase, we continue lowering the sensor to induce a preload of approximately 0.05 N. The sensor resolution and the resonant frequency are 1.5 mN and 3000 Hz, respectively. We sample the sensor reading at 10 kHz and apply a 1500 Hz non-causal low pass filter to

post-process the data. To measure the DEA's free displacement, we place a DEA under a laser vibrometer (Polytec PSV-500). The vibrometer measures the instantaneous velocity of the DEA's oscillatory motion (Extended Data Figure 2b) approximately 40 times per period. For time sequence measurements, the vibrometer averages over five cycles to reduce measurement noise. The measured velocity is integrated numerically to calculate the DEA displacement. In addition, the vibrometer can measure the DEA's frequency response by driving the DEA with white noise and computing the Fast Fourier Transform (FFT) of the displacement. This measurement gives a linear approximation of the device frequency response. It quantifies the DEA's resonant modes and phase shift (Figure 2c-d). This information is useful for robot design because the DEA's motion is approximated as linear around system resonance at flight conditions.

Sample experimental measurements of blocked force and free displacement are shown in Extended Data Figure 2c and d, respectively. In these experiments, the DEA is driven at 350 Hz and 1300 V. The amplitude of the DEA's blocked force is calculated as the maximum value of the measured force and it does not include the preload force (the range is labelled by the red arrows in Extended Data Figure 2c). In our experiments, we vary the preload in the range of 0.025 N to 0.1N and find that the magnitude of preload has a negligible effect on the blocked force measurement. The amplitude of the DEA's free displacement is calculated as the difference between the maximum and the minimum value (as indicated by the red arrows in Extended Data Figure 2d). We report the peak-to-peak displacement value because the DEA does mechanical work during both elongation and retraction. To characterize DEA performance for different operating conditions (Figure 2a-b), we vary input voltage amplitudes and driving frequencies from 800 V to 1300 V, and from 1 Hz to 600 Hz. Based on the force and displacement measurements, the actuator energy and power density are calculated as:

$$e = \frac{1}{2m_a} F_B \delta, \tag{4}$$

$$p = \frac{1}{2m_a} F_B \delta f. \tag{5}$$

Equations 4 and 5 assume the elastomer's stress-strain relationship is approximately linear. Through conducting tensile tests using an Instron materials testing machine, we find the elastomer exhibits a linear response for a strain less than 20%. The elastomer Young's modulus is measured to be 140 kPa. The maximum measured energy density (Extended Data Figure 2e) and power density (Extended Data Figure 2f) are 1.13 J/kg and 563 W/kg, respectively (at 500 Hz, 1300 V). These values satisfy the criteria for robot takeoff (Supplementary Information S1). The DEA's driving voltage can be further increased to 1500 V in controlled hovering flight demonstrations, so the DEA's peak power density is estimated to be 15% higher than the reported value. The DEA experiences dielectric breakdown for a driving voltage higher than 1500 V.

In our flight experiments, the robot is driven by an external power source through a thin tether. Here we quantify the DEA's resistance, capacitance, power consumption, and efficiency. These parameters are important for achieving power autonomous flights in future studies. To quantify the DEA's power consumption, we measure the DEA's input voltage (V) and corresponding current (I) at flight conditions. The average electrical power input is:

$$\bar{P}_{in} = \frac{1}{T}\int_0^T V(t)I(t)dt. \quad (6)$$

A sample measurement of instantaneous power is shown in Extended Data Figure 2g, in which the average power consumption is 450 mW. We further measure the DEA's resistance and capacitance by sending a step input and measuring the corresponding current response. The system is modelled as a RC circuit, and parameters such as series resistance, capacitance, and time constant can be obtained by fitting a first order system to the current response. The DEA's resistance, capacitance, and time constant are 170 kΩ, 1.04 nF, and 178 μs, respectively. Having calculated the DEA's resistance, we further compute the power dissipated due to electrical resistance:

$$\bar{P}_{ele} = \frac{R}{T}\int_0^T I^2(t)dt. \quad (7)$$

The DEA electrode dissipates 330 mW of power at flight conditions. The mechanical power output at this operating condition is calculated as $P = \frac{1}{2} F_B \delta f$, where the values of F_B, δ, and f are 0.19 N, 0.89 mm, and 300 Hz, respectively. The estimated power output is 25 mW, which implies the DEA efficiency is 5.6%. Over 73% of the power is dissipated by the electrode resistance, and the rest of the power dissipation is contributed by the elastomer's viscoelastic damping.

This power dissipation leads to substantial heating of the DEA. The system can be described by a first order conduction model:

$$\frac{dT}{dt} = -K(T - T_a) + \frac{Q}{C}, \tag{8}$$

where T is the DEA temperature, T_a is the ambient temperature, K is the dissipation rate, Q is the heat inflow, and C is the DEA's heat capacity. This first order differential equation has a closed form solution. The solutions for the rising and the cooling phases are:

$$T_{rise} = T_a + \frac{Q}{cK_1}(1 - e^{-K_1 t}), \tag{9}$$

$$T_{cool} = T_a + (T_i - T_a)e^{-K_2 t}, \tag{10}$$

where T_i is the initial temperature at the onset of cool down. The dissipation coefficients (K_1 and K_2) in the heating and the cooling phases are different because the flapping motion during the heating phase induces an airflow that facilitates convective cooling. The values of these modeling parameters are reported in Extended Data Table 1.

We use a FLIR T440 thermal camera to measure the DEA temperature when the robot operates under takeoff conditions (Extended Data Figure 2h). The DEA temperature increases from 28 ℃ to 70 ℃ in 90 seconds. An analytical fit is superimposed on the same graph (Extended Data Figure 2h). Snapshots of a thermal video are shown in Extended Data Figure 2i. The maximum DEA temperature reaches 70.0 ℃ before cool down. This experiment shows most of the input electrical power is dissipated in the form of

heat. Generating excessive amount of heat can lead to thermal failure and reduce actuator lifetime. Through our experiments, we find our DEA can operate for over 600,000 cycles under takeoff conditions, equivalent to 33 minutes of flight time.

In this study, our DEA has a low transduction efficiency of 5.6%. This low transduction efficiency would not be conducive to power autonomous flights. In addition, it requires a 1300 V driving signal to achieve takeoff, which creates challenges for developing high efficiency boost circuitry. While this study does not aim to achieve power autonomous flight, it is important to identify major challenges and potential solutions. Future studies should focus on increasing the DEA electrode's conductivity, reducing elastomer layer thickness to reduce the driving voltage, and redesigning the DEA geometry and robot wings to reduce the flapping frequency. First, increasing electrode conductivity will lead to a reduction of resistive power loss. This can be done by exploring new electrode materials such as a hybrid network of carbon nanotubes, graphene and silver nanowires[37] or intrinsically stretchable electrodes such as conductive hydrogels[38] or liquid metal. Second, reducing elastomer thickness will reduce the operating voltage. We can achieve this by increasing the spin coating speed or exploring alternative method such as using an automatic thin film applicator. Further, the spin coating and the electrode transfer process can be done in a clean room environment to reduce the number of particulates in the elastomer and on the electrodes. Third, new electroactive materials such as bottlebrush elastomers[39] can be explored to further increase the actuator's energy density. In addition, our experiments show that DEA power consumption is linearly proportional to its operating frequency. To reduce power expenditure, future studies can redesign the DEA geometry and robot transmission to reduce system resonant frequency. Alternatively, nonlinear controllers can be developed so that the DEA motion does not need to be linearized around its resonance. Beyond improving the DEAs, we can apply a new class of electrostatic actuators named Peano-HASEL[33,40] that have shown promise for achieving very high energy density and moderate bandwidth. For that class of actuators, it would be important to work on device miniaturization to reduce the driving voltage.

Methods Reference

34. Whitney, J.P., & Wood, R. J. Conceptual design of flapping-wing micro air vehicles. *Bioinspiration & Biomimetics.* **7(3),** 036001 (2012).

35. Whitney, J. P., Sreetharan, P. S., Ma, K. Y., & Wood, R. J. Pop-up book MEMS. *Journal of Micromechanics and Microengineering*. **21,** 115021 (2011).

36. Chen, Y., Ma, K., & Wood, R. J. Influence of wing morphological and inertial parameters on flapping flight performance. *In IEEE/RSJ International Conference on Intelligent Robots and Systems.* 2329-2336 (2016).

37. Liang, J., Li, L., Chen, D., Hajagos, T., Ren, Z., Chou, S. Y., Hu, W., & Pei, Q. Intrinsically stretchable and transparent thin-film transistors based on printable silver nanowires, carbon nanotubes and an elastomeric dielectric. *Nature communications*, **6**, 7647 (2015).

38. Keplinger, C., Sun, J. Y., Foo, C. C., Rothemund, P., Whitesides, G. M., & Suo, Z. Stretchable, transparent, ionic conductors. *Science*, **341**(6149), 984-987 (2013).

39. Vatankhah-Varnoosfaderani, M., Daniel, W. F., Zhushma, A. P., Li, Q., Morgan, B. J., Matyjaszewski, K., et al. Bottlebrush elastomers: A new platform for freestanding electroactuation. *Advanced Materials*, **29**(2), 1604209 (2017).

40. Kellaris, N., Venkata, V. G., Rothemund, P., & Keplinger, C. An analytical model for the design of Peano-HASEL actuators with drastically improved performance. *Extreme Mechanics Letters*, **100449** (2019).

Extended Data Figures and Tables

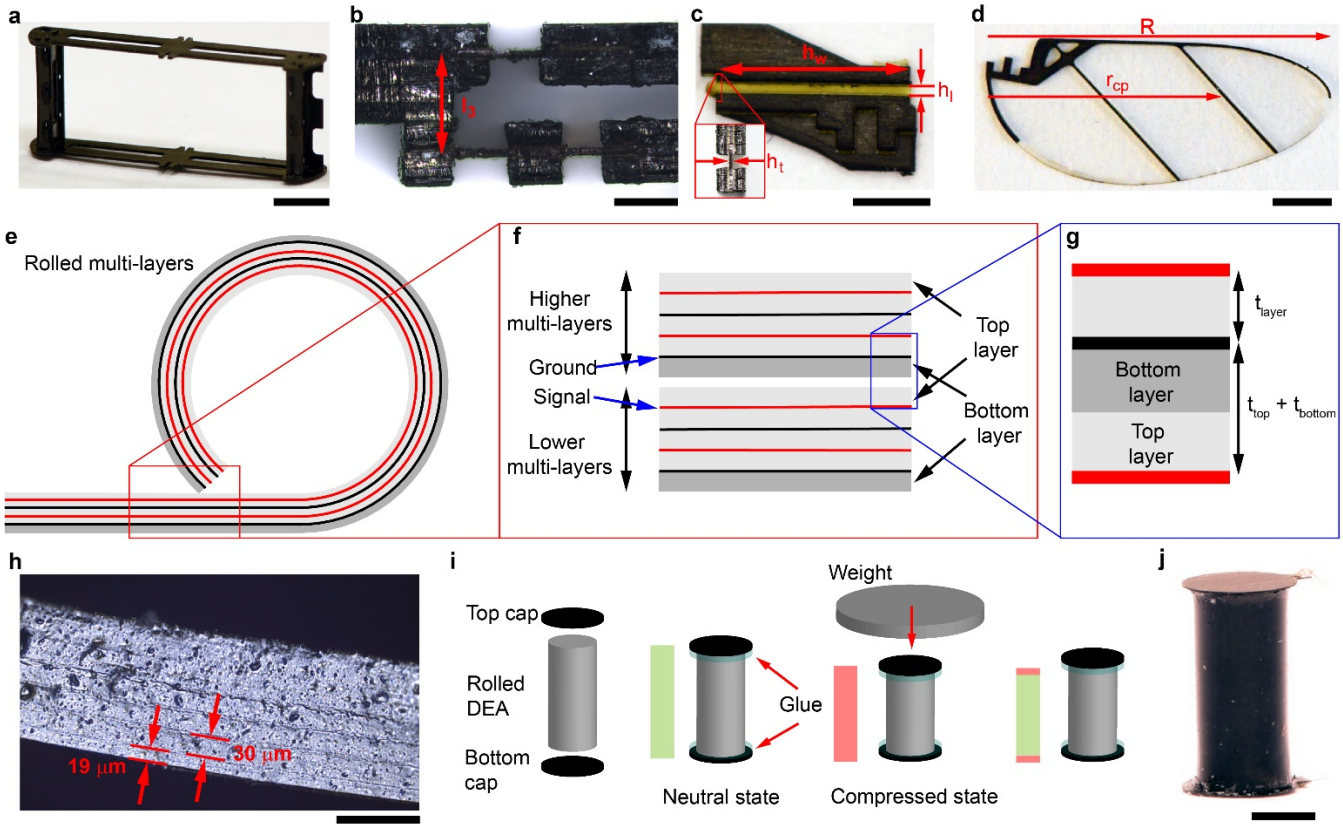

Extended Data Figure 1 | Design and fabrication of robot components. a, A 40 mg airframe made of eight pieces of carbon fiber composites. Scale bar represents 2 mm. **b,** Top view of the planar four-bar transmission. The red arrow marks l_3, which is the inverse of the transmission ratio T. Scale bar represents 200 μm. **c,** Front view of the wing hinge. The hinge width (h_w), length (h_l), and thickness (h_t) determine its torsional stiffness. Scale bar represents 1 mm. **d,** Front view of a robot wing whose wing span (R) and center of pressure (r_{cp}) are 10 mm and 7 mm, respectively. Scale bar represents 2 mm. **e**, An illustration of rolling an elastomer-electrode multilayer into a DEA. **f**, A zoomed-in illustration of the inset shown in **e**. **g**, A zoomed-in illustration of the inset shown in **f**. The bottom layer of the top multi-layer and the top layer of the bottom multi-layer forms a region that can be actuated. **h,** Confocal microscopy image of the DEA's cross section. The elastomer sheet is 220 μm thick and it has seven elastomer layers. The thickness of the top and the bottom layers are approximately 65% of the middle layers. Scale bar represents 100 μm. **i,** Fabrication of the DEA. After the elastomer sheet is rolled into a cylindrical shell, the top and bottom cap are glued onto the DEA. A weight is placed on top of the DEA as the glue cures. After the glue cures, the DEA connections remain in compression (red) while the rest of the DEA returns to its neutral state (green). **j,** Front view of a DEA. Scale bar represents 3 mm.

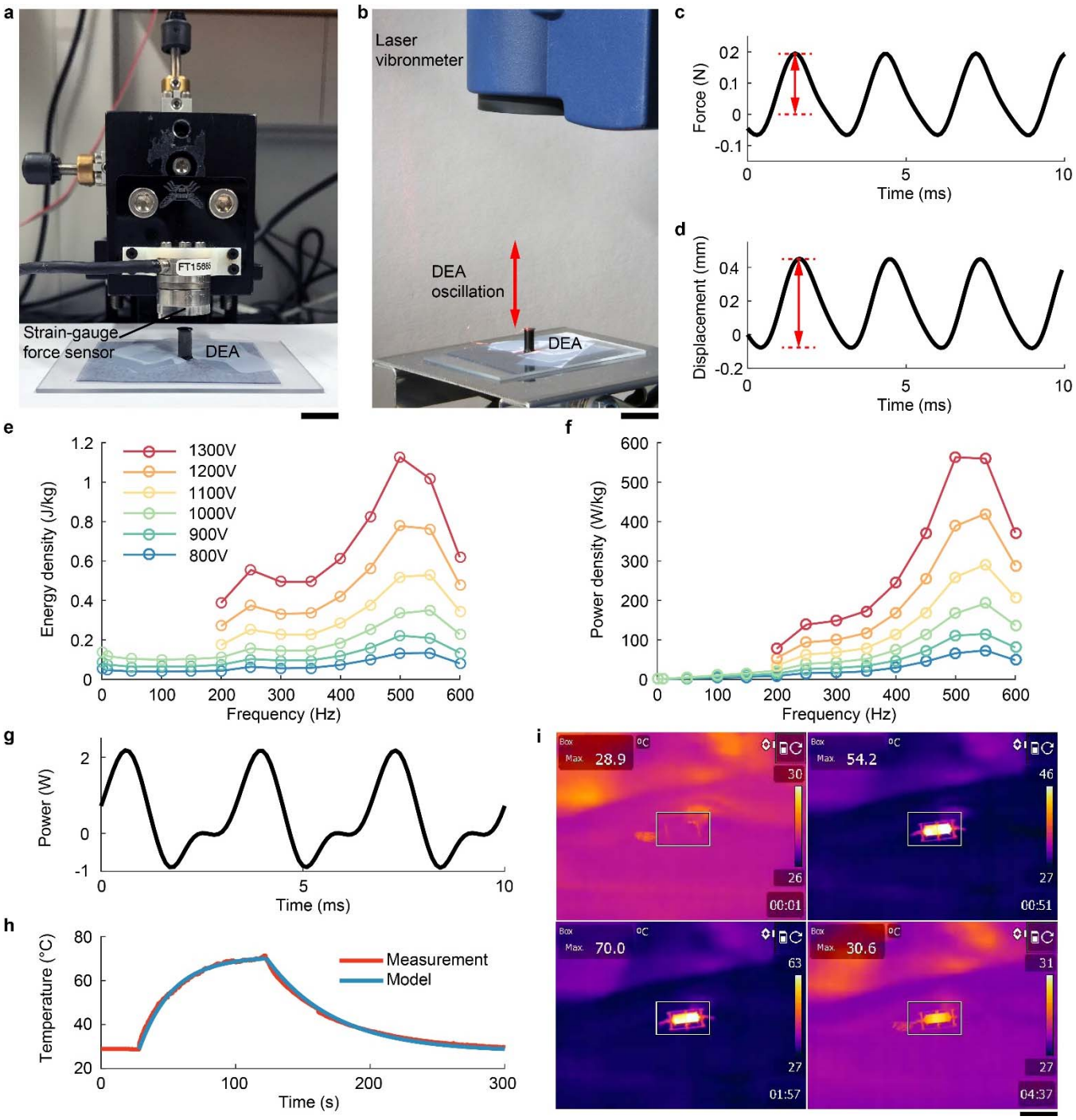

Extended Data Figure 2 | Characterization of blocked force, free displacement, and power dissipation. a, Experimental setup for measuring the DEA's blocked force. **b,** Experimental setup for measuring the DEA's free displacement. **c-d,** Sample blocked force (**c**) and free displacement (**d**) measurements when the DEA is driven at 350 Hz and 1300 V. The red arrows in **c** and **d** indicate the ranges of blocked force and free displacement that correspond to Figure 2a and b. **e-f,** The DEA's energy (**e**) and power (**f**) density as functions of driving frequency and voltage. This DEA's blocked force and free displacement measurements are shown in Figure 2**a-b. g,** The DEA's instantaneous power consumption when driven at 1400 V and 300 Hz. **h,** Measurement and modeling of the DEA's temperature profile during its operation at 1400 V and 300 Hz. **i,** Thermal images showing the temperature of the DEA during operation. **h** and **i** show the same experiment. Scale bars in (**a**, **b**, and **i**) represent 1 cm.

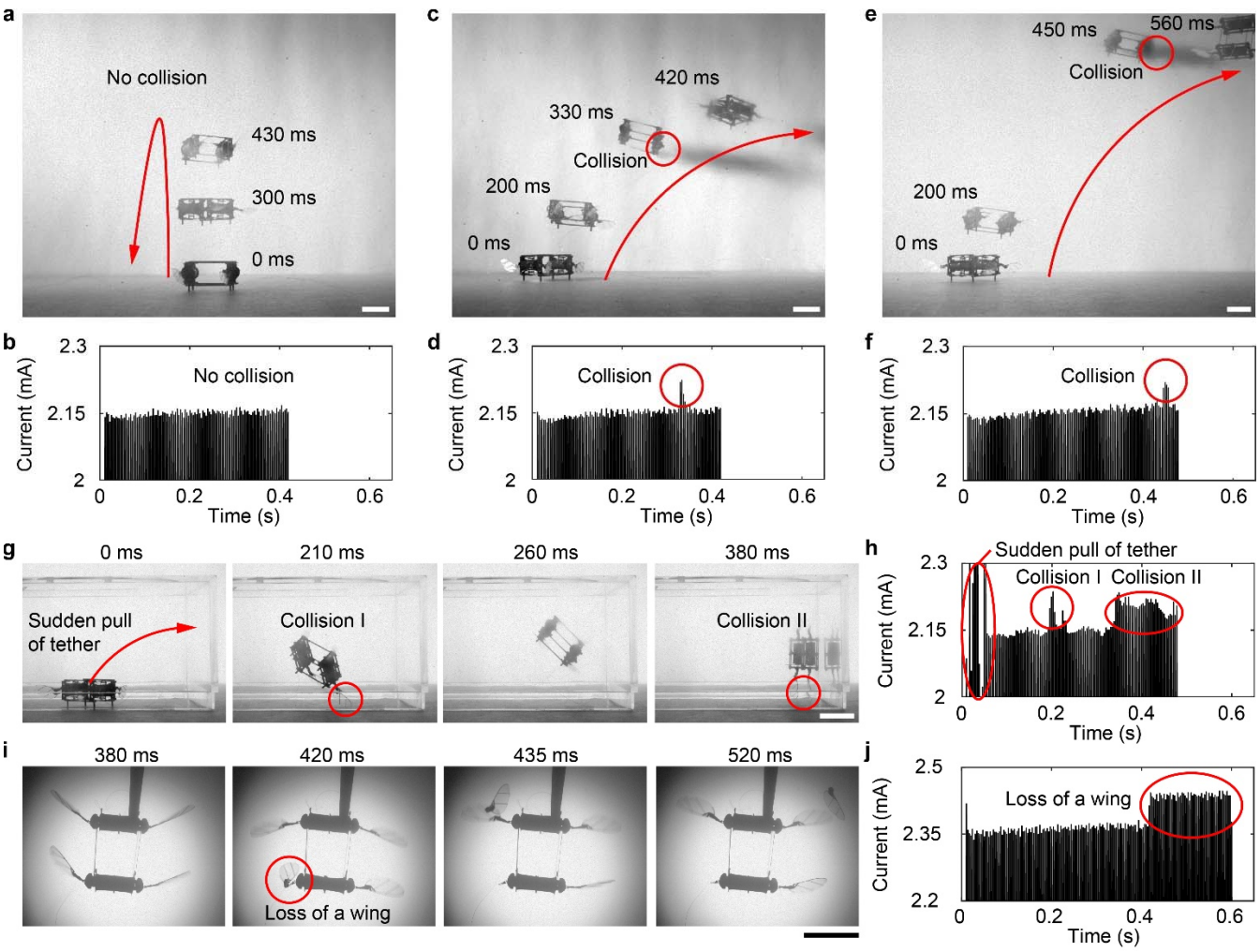

Extended Data Figure 3 | Robot in-flight collision and damage sensing. a-b, A composite image (**a**) and the measured DEA current (**b**) of a short takeoff flight without any collisions. **c-f,** Two takeoff flights in which the robot hits a wall during its ascent. The red circles in **c** and **e** mark the collision events and they correspond to the current spikes in **d** and **f,** respectively. **g-h**, A robot takeoff flight in a transparent box. The robot makes multiple collisions and the red circles in **g** and **h** relate these collisions to DEA current changes. **i-j,** An image sequence (**i**) and the measured current (**j**) of a flapping-wing characterization test. One robot wing falls off during the experiment and this event is detected by measuring the DEA current. Scale bars in (a, c, e, g, i) represent 1 cm.

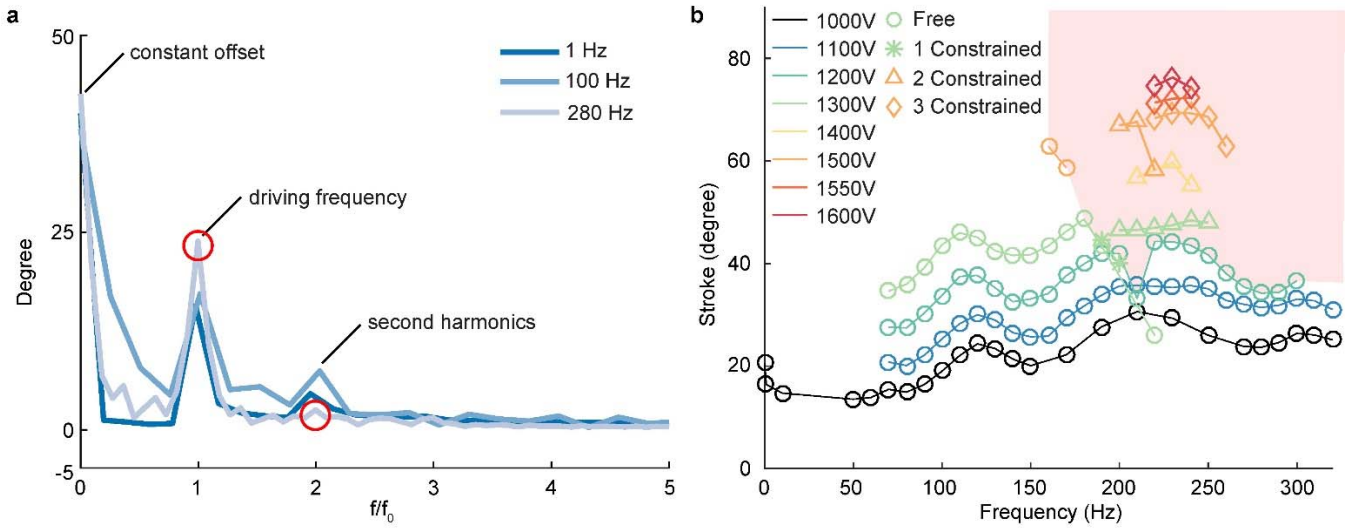

Extended Data Figure 4 | DEA actuation nonlinearity. a, Fast Fourier Transform of the tracked wing stroke kinematics when a wing is driven at 1 Hz, 100 Hz, and 280 Hz. The stroke kinematics data is taken from that shown in Figure 3b. There is a substantial second order harmonic for the cases of 1 Hz and 100 Hz. When the wing is driven near the system resonant frequency (280 Hz), the red circles indicate that the fundamental harmonic grows and the second harmonic is attenuated. **b,** Right wing stroke amplitude as a function of driving voltage and frequency. The red region represents stroke amplitudes and frequencies that cannot be achieved without constraining the DEA. This data corresponds to the same experiment shown in Figure 3f.

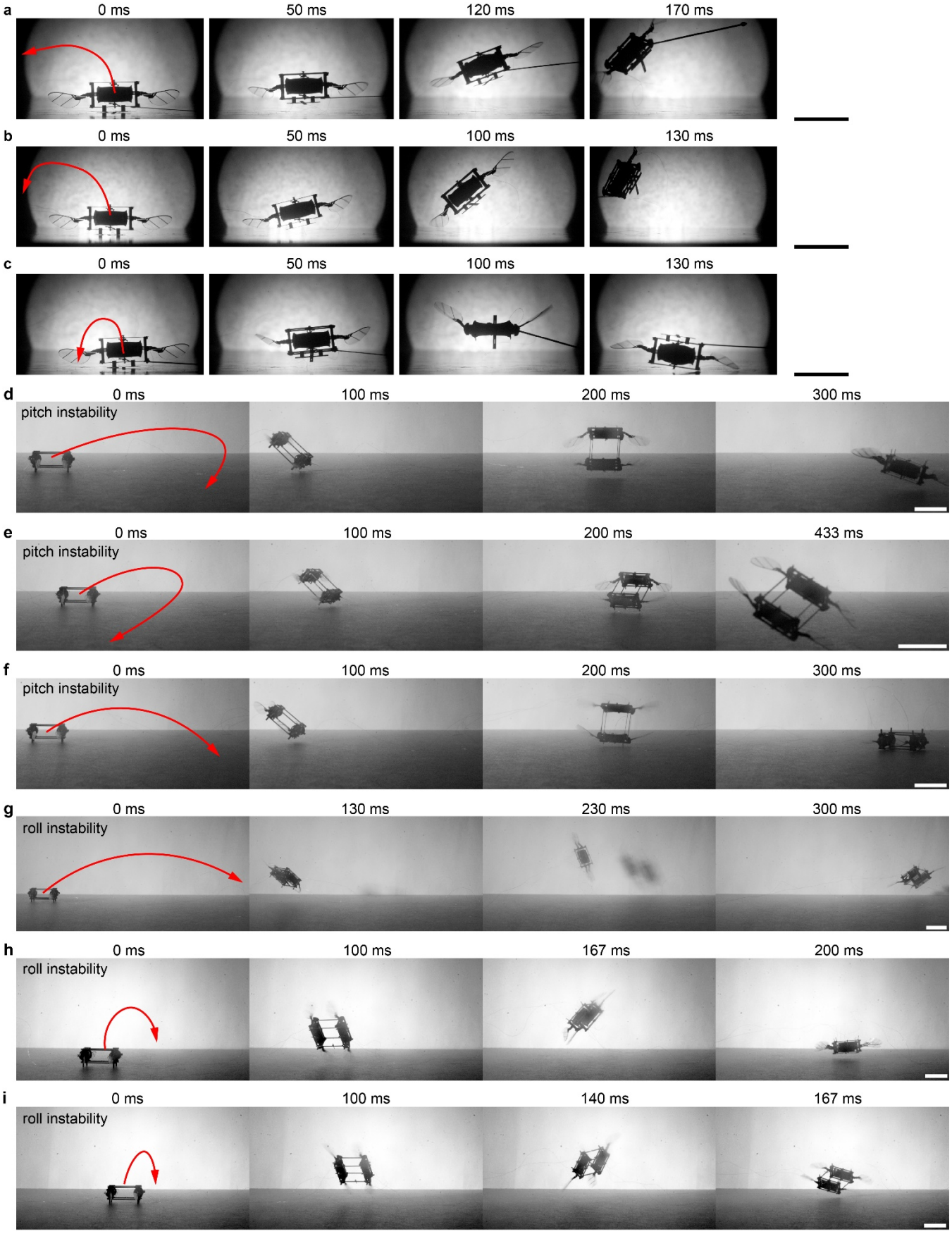
a
0 ms
50 ms
120 ms
170 ms
b
0 ms
50 ms
100 ms
130 ms
c
0 ms
50 ms
100 ms
130 ms
d
0 ms
100 ms
200 ms
300 ms
pitch instability
e
0 ms
100 ms
200 ms
433 ms
pitch instability
f
0 ms
100 ms
200 ms
300 ms
pitch instability
g
0 ms
130 ms
230 ms
300 ms
roll instability
h
0 ms
100 ms
167 ms
200 ms
roll instability
i
0 ms
100 ms
140 ms
167 ms
roll instability

603

Extended Data Figure 5 | Repeated unstable takeoff flights. (a-c), Three takeoff flights of a robot with one DEA. In these flights, the robot flips upside down within 200 ms after liftoff due to aerodynamic torque imbalances from the two wings. **(d-i),** Unstable takeoff flights of a robot with two DEAs. In (**d-f**), the robot pitches forward and eventually flips over due to asymmetric lift forces from the front and the back robot modules. In (**g-i**), the robot rolls sideways and flips over due to lift force imbalances between its left and right wings. Scale bars in (**a-i**) represent 1 cm.

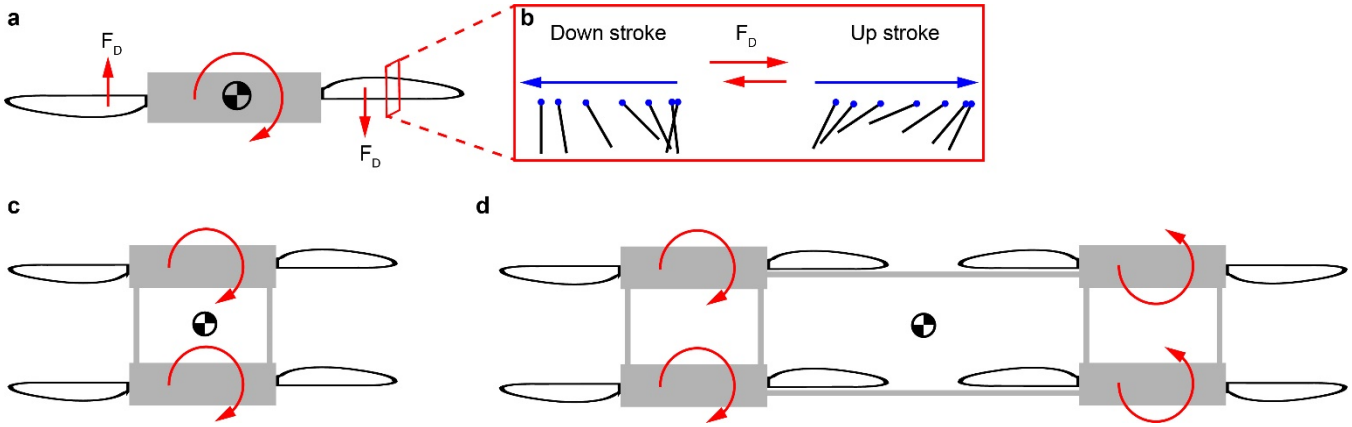

Extended Data Figure 6 | Illustration of robot yaw torque generation through biasing the mean wing pitch angle. a, Illustration of wing pitch bias in an one-DEA module. The red arrows indicate the directions of the mean drag force due to biasing the wing pitch. The net drag forces from the two wings induce a robot yaw torque. **b**, The inset shows the motion of a wing chord on a 2D plane. The wing pitch bias causes different wing pitching motion in the up stroke and down stroke phases of the wing motion, which leads to different drag forces. **c,** Two one-DEA modules having the same yaw torque bias direction are assembled into a two-DEA robot. **d,** Two two-DEA modules having opposite yaw torque bias directions are assembled into a four-DEA robot.

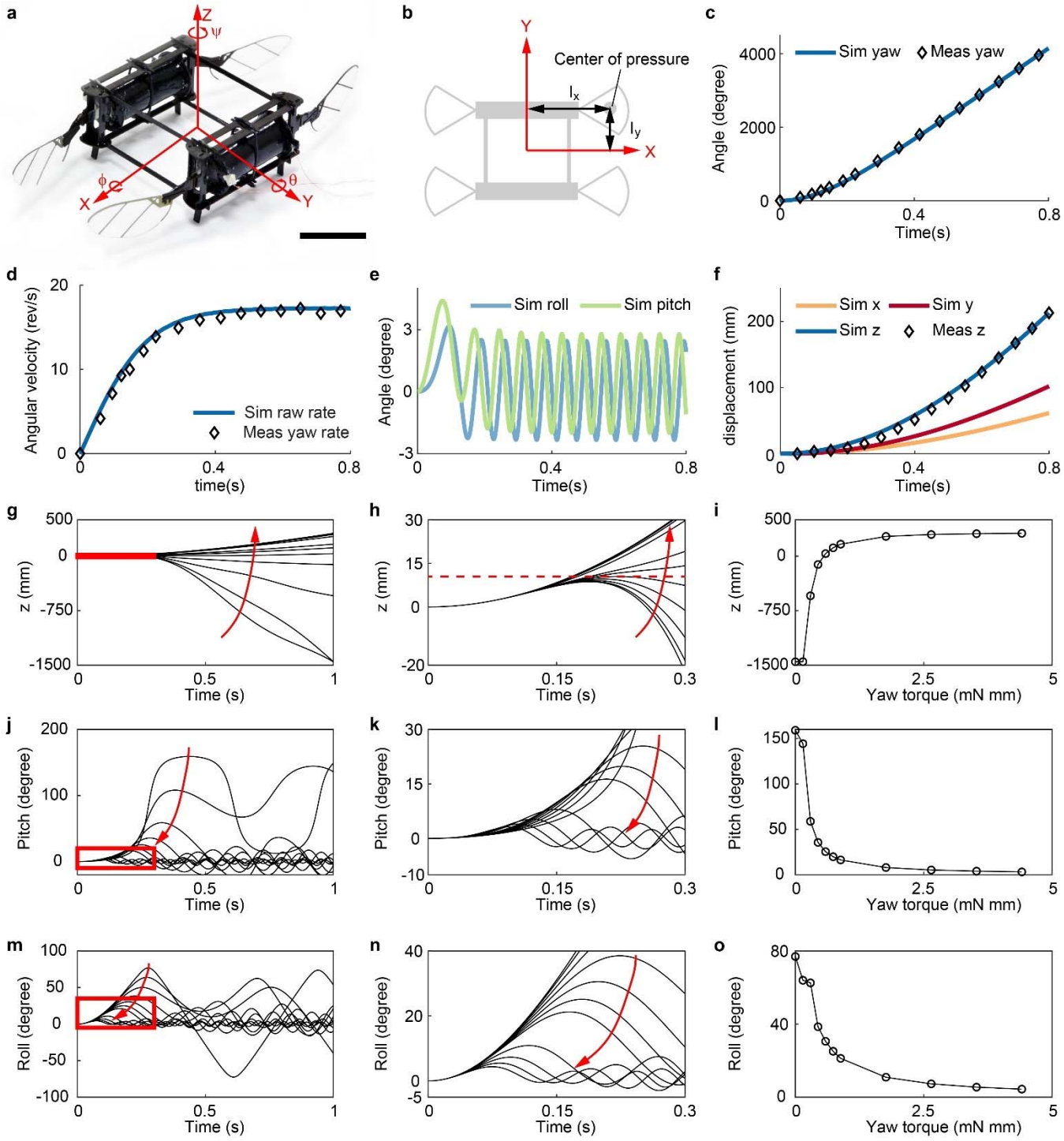

Extended Data Figure 7 | Simulation of open-loop ascending flight and comparison with experimental results. a, Coordinate system definition of the four-wing robot model. Scale bar represents 1 cm. **b,** Top view schematic of the four-wing robot. l_x and l_y denote the distance from the robot's center of mass to each wing's center of pressure. **c,** Comparison of measured and simulated yaw (ψ) motion. The robot makes 11 revolutions with respect to its z-axis 0.8 s after takeoff. **d,** Comparison of measured and simulated yaw rate ($\dot{\psi}$). The steady state angular velocity of the robot's yaw rate is 17.5 revolutions per second. **e,** Simulated roll (ϕ) and pitch (θ) motion. Our simulation predicts that the steady state oscillation with respect to the robot's X and Y axes is smaller than 3°. **f,** Simulation results of the robot's displacement

after takeoff. The experimental measurement of the robot's vertical motion is superimposed on the same graph. The data shown in (**c**-**f**) correspond to the same simulation and experiment shown in Supplementary Video 5 and Figure 4b-c. **g**-**o**, Dynamical simulation of robot takeoff flights under different values of body yaw torque. **g,** Robot altitude as a function of time. **h,** A zoomed-in plot of robot altitude shortly after takeoff. This plot corresponds to the red region in **g**. **i,** Robot altitude at one second after takeoff as a function of input body yaw torque. **j**, Robot pitch motion as a function of time. **k**, A zoomed-in plot of robot pitch that corresponds to the red region in **j**. **l,** Maximum robot pitch deviation as a function of input yaw torque. **m**, Robot roll motion as a function of time. **n**, A zoomed-in plot of robot roll that corresponds to the red region in **m**. **o**, Maximum robot roll deviation as a function of input yaw torque.

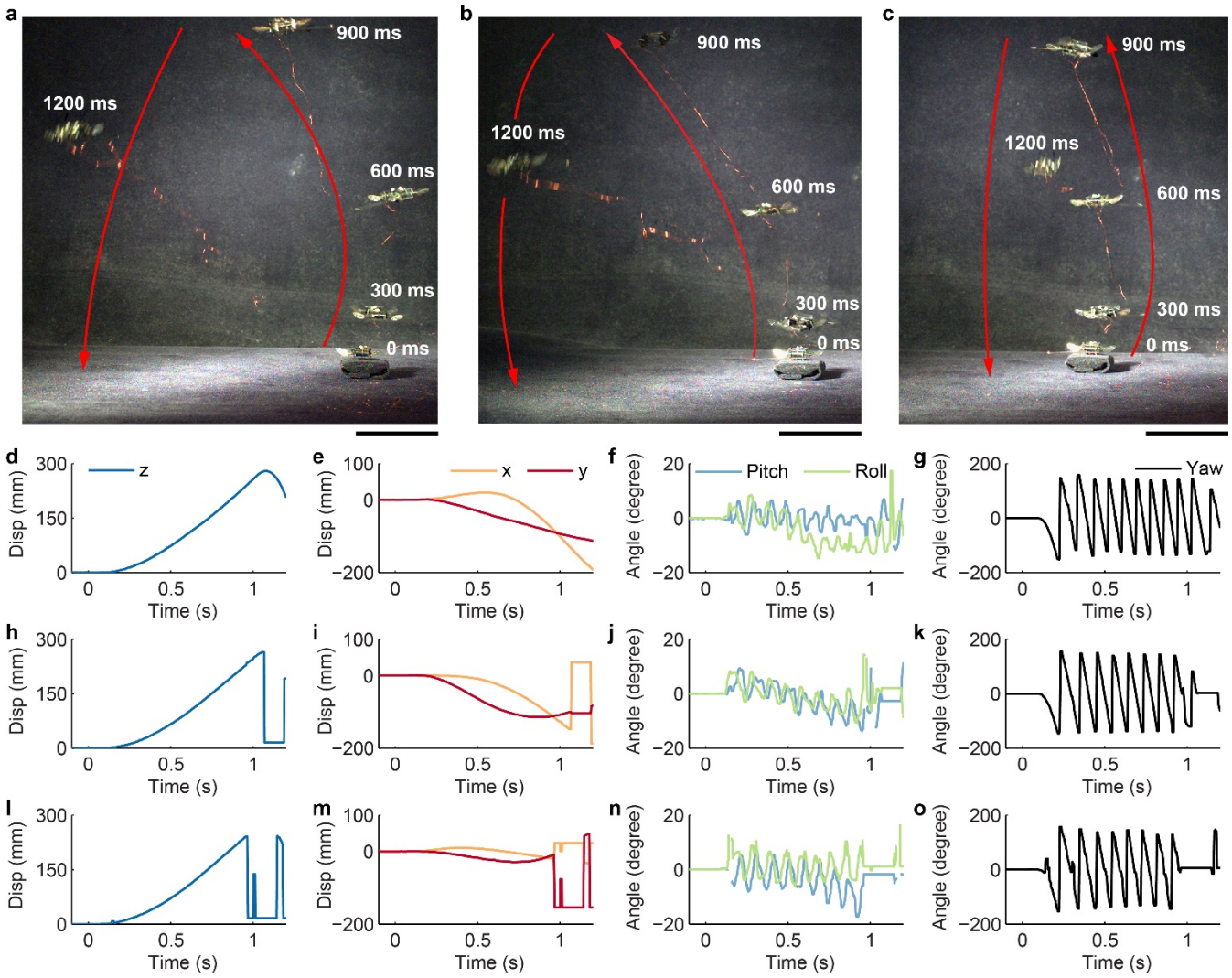

Extended Data Figure 8 | Three passively stable ascending flights of a robot with two DEAs. a-c, Composite images of three one-second, open-loop ascending flights. **d-g**, Tracked robot altitude (**d**), x and y center of mass position (**e**), pitch and roll orientation (**f**), and yaw rotation (**g**). The data shown in **d-g** correspond to the flight shown in **a**. Similarly, (**h-k**) and (**l-o**) show the tracked flight data corresponding to the flights shown in **b** and **c**, respectively. Sudden jumps in the tracking data (**h**, **i**, **l**, and **m**) indicate the time at which the Vicon motion capture system loses tracking.

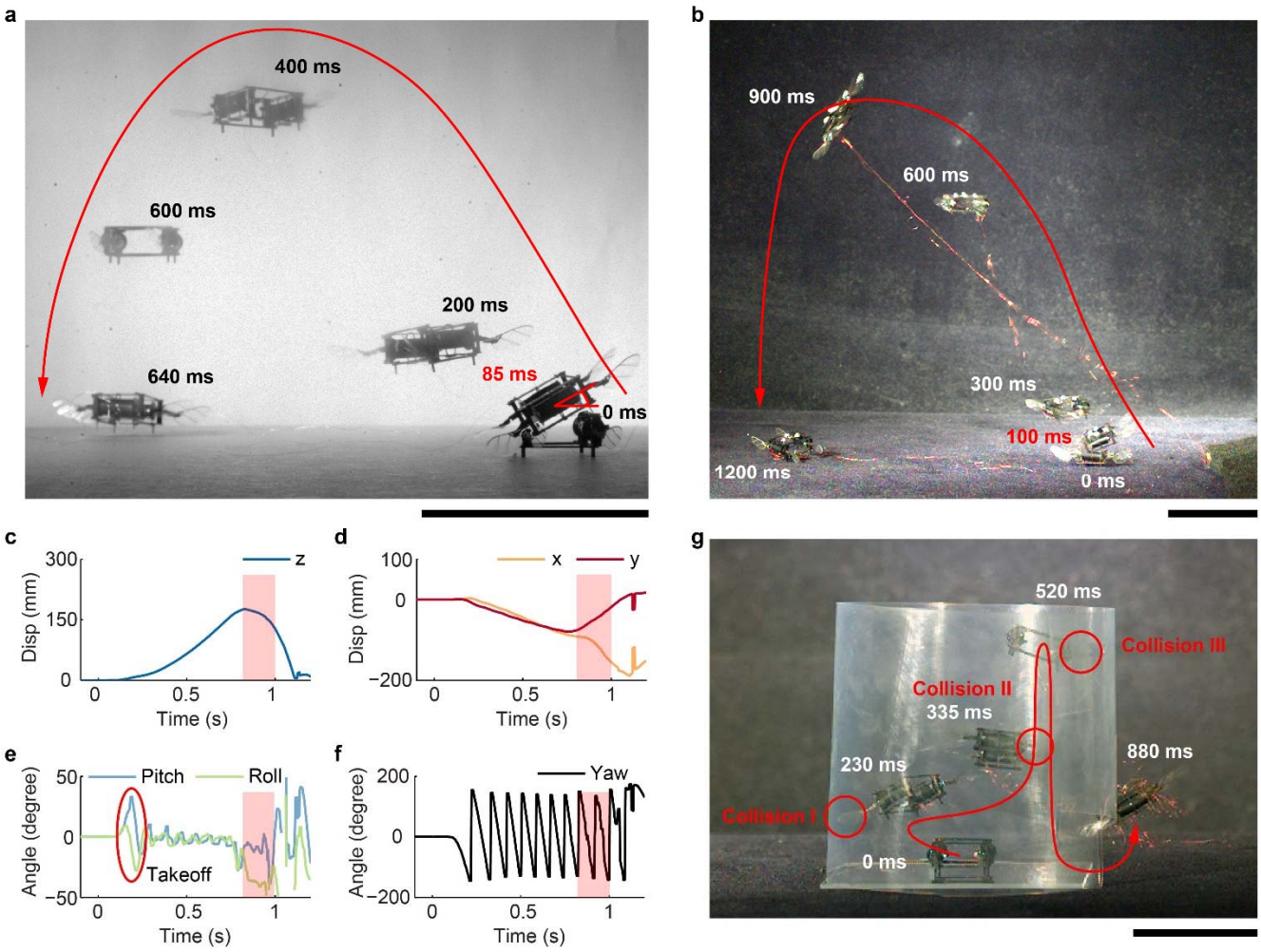

Extended Data Figure 9 | Robot unbalanced takeoff flights and a failed collision recovery experiment. a, A composite image of a 0.5 second open-loop takeoff flight captured at 3000 frames per second. The robot pitch deviation is approximately 35 degree 85 ms after takeoff. **b**, A composite image of a 1 second open-loop takeoff flight conducted in the Vicon motion tracking arena. **c-f**, Tracked robot altitude (**c**), x and y center of mass position (**d**), pitch and roll orientation (**e**), and yaw rotation (**f**). The data shown in **c-f** correspond to the flight in **b**. The red circle in **e** illustrates the large robot pitch and roll deviation after takeoff. The red shaded region in **c-f** show the changes of robot position and orientation after it is pulled by its tether. **g**, An example of a failed collision recovery experiment. The robot is destabilized after making the third collision. Scale bars in **a**, **b**, and **g** represent 5 cm.

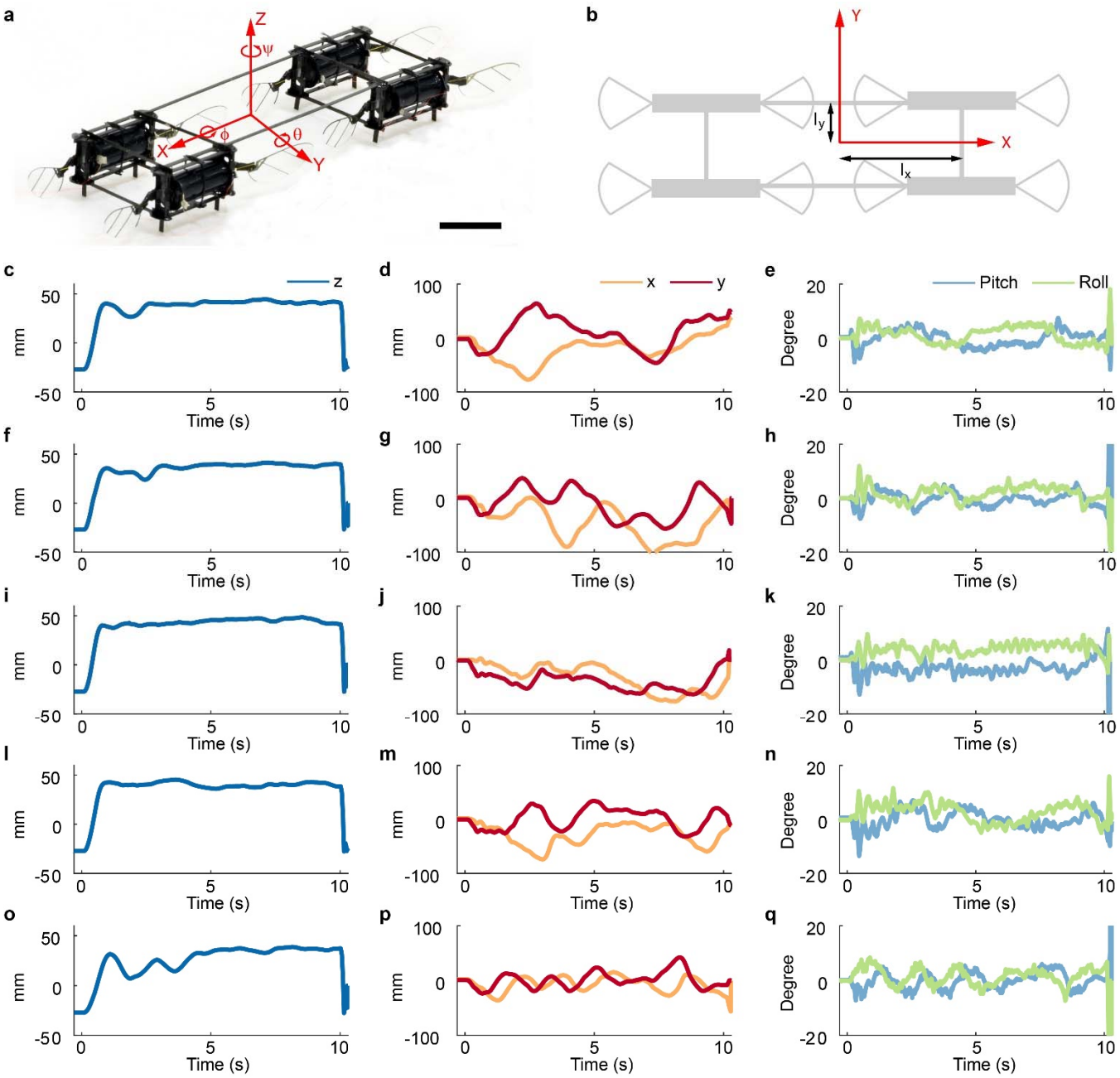

Extended Data Figure 10 | Controller design of the eight-wing robot and hovering flight repeatability. a, Perspective view of the eight-wing robot with a superimposed coordinate system. The roll (ϕ), pitch (θ), and yaw (ψ) angles are defined with respect to the fixed *X*, *Y*, and *Z* axes. Scale bar represents 1 cm. **b,** Top view schematic of the eight-wing robot. l_x and l_y denote the distance from the robot center of mass to the geometric center of each DEA. **c-q**, Tracked robot position and attitude data of five 10-second hovering flights. In these flights, we do not control the robot's yaw motion. **(c, f, i, l, o),** The first column shows the robot's altitude as a function of time. **(d, g, j, m, p),** The second column shows the robot's lateral position as a function of time**. (e, h, k, n, q),** The last column shows the robot's roll (ϕ) and pitch (θ) motion as a function of time.

Extended Data Table 1 | Parameters for the conceptual design of the two-wing robot.

Parameter	Symbol	Value
Robot mass	m	160 mg
Mean drag coefficient	$\overline{C_D}$	1.6
Mean lift coefficient	$\overline{C_L}$	0.7
Transmission ratio	T	2530 rad·m^{-1}
Maximum lift to weight ratio	f_m	1.2
Robot transmission dimensions	t, w, l	25 μm, 1.2 mm, 200 μm
Young's modulus of polyimide film	E	2.5 GPa
Wing aspect ratio	AR	3
Wing span	R	9.9 mm
Wing span wise moment of inertia	I_{zz}	15 mg·mm^2
Wing span wise center of pressure	r_{cp}	7 mm
Air density	ρ	1.2 kg·m^{-3}
Wing hinge geometry	t_h, w_h, l_h	7.5 μm, 2.65 mm, 110 μm
DEA mass	m_a	100 mg
DEA natural resonance frequency	f_{res}	465 Hz
Heat generated during operation	Q	0.25 J·s^{-1}
DEA heat capacity	C	0.15 J·K^{-1}
Ambient temperature	T_a	28.7 °C
Initial temperature at onset of cooling	T_i	70 °C
Heat conduction rate during heating	K_1	0.04 s^{-1}
Heat conduction rate during cooling	K_2	0.022 s^{-1}

Extended Data Table 2 | Physical and simulation parameters for the four-wing robot. These parameter values correspond to the simulation results shown in Extended Data Figure 7.

Parameter	Symbol	Value
Mass	m	320 mg
Principal moment of inertia	I_{xx}, I_{yy}, I_{zz}	2.99×10^4, 2.41×10^3, 3.13×10^4 mg·mm^2
Distance to robot center of mass	l_x, l_y	13.3, 7 mm
Lift force of each wing	$F_{L1}, F_{L2}, F_{L3}, F_{L4}$	0.86, 0.81, 0.82, 0.88 mN
Drag force of each wing	$F_{D1}, F_{D2}, F_{D3}, F_{D4}$	0.29, 0.29, 0.29, 0.29 mN
Body damping force coefficient	b_f	0.5 mg·mm^{-1}
Body damping torque coefficient	b_t	1.5×10^3 mg·mm^2

Extended Data Table 3 | Values of flight controller parameters for hovering flights corresponding to Figure 4e-i and Extended Data Figure 10.

#	Flight duration (s)	λ_0 (s^{-4})	λ_1 (s^{-3})	λ_2 (s^{-2})	λ_3 (s^{-1})	Λ_0 (s^{-2})	Λ_1 (s^{-1})	α (V/mN)	β (V)	$\gamma_1, \gamma_2, \gamma_3, \gamma_4$ (V)
1	10	13608	6631	798	62	25	125	82	1172	38, 80, 69, 34
2	10	13608	6631	798	62	25	125	82	1172	38, 80, 69, 34
3	10	27216	9946	570	57	25	125	82	1172	38, 80, 69, 34
4	10	30618	9946	570	57	25	125	82	1172	38, 80, 69, 34
5	10	54432	13262	713	71	25	125	82	1172	38, 80, 69, 34
6	16	54432	13262	713	71	30	150	82	1172	38, 85, 74, 34